

On the relation between magnetic field strength and gas density in the interstellar medium: A multiscale analysis

D. J. Whitworth,^{1,2,3*} S. Srinivasan,¹ R.E. Pudritz,^{3,4} M.-M. Mac Low,⁵ R. J. Smith,⁶ A. Palau,¹ K. Pattle,^{7,8} G. Eadie,^{9,10,11} H. Robinson,⁴ R. Pillsworth,⁴ J. Wadsley,⁴ N. Brucy,³ U. Lebreuilly,¹² P. Hennebelle,¹² P. Girichidis,³ F. A. Gent,^{13,14} J. Marin,² L. Sánchez Valido,^{15,5} V. Camacho,¹ R. S. Klessen,^{3,16} and E. Vázquez-Semadeni¹

¹Universidad Nacional Autónoma de México, Instituto de Radioastronomía y Astrofísica, Antigua Carretera a Pátzcuaro 8701, Ex-Hda. San José de la Huerta, 58089 Morelia, Michoacán, México

²Jodrell Bank Centre for Astrophysics, Dept. of Physics and Astronomy, University of Manchester, Oxford Road, Manchester M13 9PL, UK

³Universität Heidelberg, Zentrum für Astronomie, Institut für Theoretische Astrophysik, Albert-Ueberle-Str. 2, 69120 Heidelberg, Germany

⁴Department of Physics and Astronomy, McMaster University, 1280 Main Street West, Hamilton, ON, L8S4K1, Canada

⁵Department of Astrophysics, American Museum of Natural History, 200 Central Park West, New York, NY 10024, USA

⁶SUPA, School of Physics and Astronomy, University of St Andrews, North Haugh, St Andrews, KY16 9SS, UK

⁷Department of Physics and Astronomy, University College London, Gower Street, London WC1E 6BT, United Kingdom

⁸Centre for Astronomy, School of Natural Sciences, University of Galway, University Road, Galway H91 TK33, Ireland

⁹David A. Dunlap Department of Astronomy & Astrophysics, University of Toronto, 50 St George St, Toronto, ON, M5S 3H4, Canada

¹⁰Department of Statistical Sciences, University of Toronto, 700 University Avenue, Toronto, ON M5G 1Z5, Canada

¹¹Data Sciences Institute, University of Toronto, 700 University Avenue, Toronto, ON, M5G 1Z5, Canada

¹²Université Paris-Saclay, Université Paris Cité, CEA, CNRS, AIM, 91191, Gif-sur-Yvette, France

¹³Astroinformatics, Department of Computer Science, Aalto University, PO Box 15400, FI-00076, Espoo, Finland

¹⁴Nordita, KTH Royal Institute of Technology and Stockholm University, Hannes Alfvéns väg 12, Stockholm, SE-106, Sweden

¹⁵Department of Physics & Astronomy, Barnard College, Altschul Hall 504A, 3009 Broadway, New York, NY 10027, USA

¹⁶Universität Heidelberg, Interdisziplinäres Zentrum für Wissenschaftliches Rechnen, Im Neuenheimer Feld 205, 69120 Heidelberg, Germany

Accepted XXX. Received YYY; in original form ZZZ

ABSTRACT

The relation between magnetic field strength B and gas density n in the interstellar medium is of fundamental importance to many areas of astrophysics, from protostellar disks to galaxy evolution. We present and compare Bayesian analyses of the $B - n$ relation for a comprehensive observational data set, as well as a large body of numerical MHD simulations. We extend the original Zeeman relation of Crutcher et al. (2010) with a large body of magnetic data that includes 700 observations with the Davis-Chandrasekhar-Fermi method. By using a new multi-parameter Bayesian analysis we present a new, more general, time-averaged observational relation: $B \propto n^{0.27 \pm 0.017}$ for $n \leq n_0$ and $B \propto n^{0.54 \pm 0.18}$ for $n > n_0$, with $n_0 = 924^{+145}_{-144} \text{ cm}^{-3}$. We perform a separate analysis on 19 numerical magnetohydrodynamics simulations that cover a wide range of scales, resolutions, initial conditions, and completed with a variety of codes: AREPO, FLASH, PENCIL, and RAMSES. The power law exponents derived from the simulations depend on several physical factors including: dynamo effects, time scales, turbulence, and the initial seed field strength. In particular, early-time simulations where the density, velocity and magnetic fields are unevolved do not match the observational scalings. The simulations that trace the observed density range best, the evolved dwarf galaxy and Milky Way like galaxy simulations, settle into a near consistent exponent of $\simeq 0.5$ in the dense gas, with variability in the diffuse gas exponent.

Key words: ISM: magnetic fields – Magnetohydrodynamics (MHD)

1 INTRODUCTION

The connection between magnetic fields and star formation has been debated ever since the discovery of interstellar magnetic fields over 70 years ago (Davis 1951). Since that time, magnetic fields have been discovered in a wide variety of

* E-mail: d.whitworth@irya.unam.mx

astrophysical systems including galaxy clusters (e.g. Carilli & Taylor 2002), spiral galaxies (e.g. Beck 2015), the diffuse interstellar medium (ISM), giant molecular clouds (e.g. Crutcher 2012), regions of star cluster formation (e.g. Pudritz et al. 2014; Kirk et al. 2015), and protostellar discs (e.g. Hull & Zhang 2019). It is well-recognised that magnetic fields may play a significant role in gas dynamics across many decades of physical scale which have very different properties. As an example, the question of their connection to the ISM and whether or not they support giant molecular clouds against collapse and affect star formation drives major observational programs (See for example: Crutcher et al. 2010; Pillai et al. 2015; Planck Collaboration et al. 2016; Soler 2019) and numerical simulations (See for example: Girichidis et al. 2018; Gent et al. 2021; Bracy et al. 2023; Robinson & Wadsley 2023; Whitworth et al. 2023; Zhao et al. 2024) of ever growing sophistication and resolution.

Mestel (1966) first proposed a theoretical connection between magnetic field strength and density in studies of the collapse of dense, magnetised, gravitationally bound clouds. He suggested two possible power-law relationships of the form $B \propto n^\alpha$, depending on the strength of the field. In the case of weak fields, the morphology of the cloud is unaffected so that the field is dragged in kinematically in a spherical or isotropic collapse, yielding $|\mathbf{B}| \propto n^{2/3}$ (hereafter called the 'kinematic' model). However, stronger fields dynamically constrain the gas to collapse parallel to field lines, giving rise to a $|\mathbf{B}| \propto n^{1/2}$ (hereafter called the 'dynamic' model) scaling. In the dynamical case clouds become more elongated and flattened as they follow the field lines (Mouschovias 1976; Mouschovias & Ciolek 1999).

The B - n relation is far more general and plays an important role in a larger set of astrophysical environments. Turbulence drives dynamo action that establishes field strengths in media of widely different densities, from the diffuse ISM, to the denser portion of molecular clouds. Earlier work (Paszot & Vázquez-Semadeni 2003) showed that in turbulent MHD simulations without self-gravity the relationship between magnetic pressure, B^2 , and density depends on the type of MHD wave mode predominantly active in the flow, as the fast mode produces a scaling $B^2 \propto n^2$, while the slow mode produces a scaling $B^2 \propto c_1 - c_2 n$, where c_1 and c_2 are constants. This was backed up by Gent et al. (2021) who showed that the small-scale dynamo (SSD) is driven to saturation in a multiphase, turbulent diffuse medium. It is therefore important to encompass a much broader range of dynamical simulations for the B - n relation and to compare these with the most comprehensive observational data sets available.

In a seminal paper, Crutcher et al. (2010) compiled Zeeman measurements of magnetic field strengths from a variety of published data sets. Low density gas measurements were acquired from HI and OH lines, whereas higher gas densities used OH and CN lines. Their Bayesian analysis of Zeeman measurements of 137 molecular clouds yielded a kinematic power-law relation of $B \propto n^{2/3}$ above densities of $n = 300 \text{ cm}^{-3}$, while below this density the relationship was interpreted as being flat, i.e. $B \propto n^0$. This power-law coefficient derived by Crutcher et al. (2010) suggests that magnetic energy does not dominate against gravity at intermediate to high densities. This has been supported by some subsequent observations (Soler 2019) and is seen in theoretical simula-

tions (Seifried et al. 2020; Ibáñez-Mejía et al. 2022; Whitworth et al. 2023).

Other work gives different results. For example Tritsis et al. (2015) reanalysed the Zeeman data used by Crutcher, and showed that with relaxed assumptions on the errors a smaller index is found, with $B \propto n^{1/2}$ being more likely. On the other hand, Jiang et al. (2020) show a larger exponent of $\alpha \sim 0.72$ and argue that due to the observational uncertainties on both B and n it is difficult to accurately determine the exponent and density at which the turn over occurs.

An important recent development in the field is that observational data sets have been greatly expanded with submillimeter polarization measurements in denser regions using instruments like the Submillimeter Array (SMA). Using a combination of the scatter of polarization directions and the velocity dispersion, the local field strength can be estimated in the gas via the Davis-Chandrasekhar-Fermi (DCF) method (Davis 1951; Chandrasekhar & Fermi 1953).

The main assumptions of the DCF method are: 1) that there is an underlying uniform magnetic field perturbed by the gas turbulent motions, 2) that the dispersion in polarization position angles, σ_{PA} , is produced by the propagation of incompressible MHD waves (i.e., Alfvén waves), and 3) that the gas kinetic energy (which is assumed to be fully turbulent) is completely transferred to magnetic energy fluctuations. The DCF method allows us to relate the gas density ρ , the velocity dispersion σ_v , and polarization angle dispersion σ_{PA} to the plane-of-sky component of the magnetic field, B_{pos} (in cgs units),

$$B_{\text{pos}} = f \sqrt{4\pi\rho} \frac{\sigma_v}{\sigma_{PA}}, \quad (1)$$

where f is a correction factor further discussed below.

One potential source of uncertainty in the DCF method is that whereas it has been generally assumed that σ_{PA} is produced by the propagation of incompressible MHD waves, compressible modes of turbulence could also have a significant contribution. Skalidis & Tassis (2021) (henceforth ST) and Skalidis et al. (2021) develop a new method to take the compressible modes into account, implying equipartition between the coupling term magnetic energy and the turbulent kinetic energy. This method is new and has yet to be rigorously tested observationally and numerically but the early results are promising.

The advent of powerful magnetohydrodynamics (MHD) codes has allowed the simulation of a wide variety of regions in the ISM, from protostellar discs to entire galaxies. In general, these have shown that up to densities of 10^5 cm^{-3} , ideal MHD applies: the field is tied to the flow of the gas as the effects of ambipolar diffusion are subdominant (e.g. Mac Low & Klessen 2004). For galaxy scale simulations this is sufficient as they do not resolve down to scales where these effects become important. Simulations that model protostellar discs (Lebreuilly et al. 2021) and individual star formation (Moscadelli et al. 2022) include non-ideal MHD physics at densities where ambipolar diffusion becomes important.

This large body of numerical work is now adding to our understanding of the B - n relation. On the scale of dwarf galaxies Whitworth et al. (2023) reported a relationship of $|\mathbf{B}| \propto n^{1/2}$ in high resolution simulations. Other theoretical work also shows a similar exponent (Hennebelle et al. 2008; Banerjee et al. 2009; Girma & Teyssier 2023). However in different

simulations the B - n relation can vary depending on numerous conditions such as initial seed field strength (Robinson & Wadsley 2023), dynamo effects (Gent et al. 2024; Korpi-Lagg et al. 2024), embedded ISM dynamics (Ibáñez-Mejía et al. 2022) and time dependencies (Robinson & Wadsley 2023; Konstantinou et al. 2024). These can all affect whether a break in the relation appears at some density, and value of the exponents.

These new observational data and the growing body of MHD simulations across many different physical scales in the ISM prompt two basic questions. Is there a general density-magnetic field relation in the ISM? If so, then what is driving it? In this work we present a new multi-scale, Bayesian statistical analysis of this relationship both for an extended set of observations as well as a wide range of current numerical simulations.

The structure of the work is as follows: Section 2 briefly describes the methods used in our analysis; Section 3 shows the results from recent observations; Section 4 shows the results from multiple, state-of-the-art numerical simulations using different initial conditions and codes; Section 5 discusses the results and compares the observational results to the numerical results; while Section 6 summarises our findings.

2 METHOD

In this section we briefly describe our methods. We first introduce the functional form we assume for the B - n relation (Sect. 2.1) and describe our Bayesian analysis in Section 2.2; Appendix A provides a more detailed description of the analysis and error treatment. We then outline the data sets (both observational and numerical) used in this study, along with their uncertainties in Sections 2.3 and 2.4.

2.1 Functional Form

In order to compare and contrast with the original Crutcher et al. (2010) relation, we assume a two-part broken power-law B - n relation for our model, similar to theirs;

$$|\mathbf{B}| = B_0 \begin{cases} (n/n_0)^{\alpha_1} & \text{if } n \leq n_0, \\ (n/n_0)^{\alpha_2} & \text{if } n > n_0. \end{cases} \quad (2)$$

where α_1 and α_2 are the exponents of the two power-laws, n_0 is the number density of the break in the power-law, and B_0 is the magnetic field strength at the break. These four variables are the free parameters for our Bayesian model, along with $\ln V$, a nuisance factor applied to the errors to take into account the intrinsic variance of the data and systematic errors. Our model differs from Crutcher et al. (2010) in that we include the five free parameters listed above rather than three and do not consider a maximum on B but use the reported values in their respective publications. We discard the flexibility function free parameter that was used in Crutcher et al. (2010) which denotes the trust in the PDF used in the prior.

Crutcher et al. (2010) found that above a density of $n_0 = 300 \text{ cm}^{-3}$, $\alpha_2 \simeq 0.65$. This power law scaling is expected if spherical magnetised clouds are compressed, which gives $|\mathbf{B}| \propto n^{2/3}$.

With the addition of more data we now have many more

points across a larger density range, up to $n \simeq 10^9 \text{ cm}^{-3}$. Patte et al. (2022) note that at densities of $n > 10^7 \text{ cm}^{-3}$ the field strength appears to flatten, as can be seen in the figures to come. However, we refrain from a three value power-law because much of this high density data lacks errors and so can not be fitted with MCMC. More importantly, at these densities the DCF method becomes unreliable for various reasons. For example, in this regime it is expected that dust grains will align more to the radiation field than to the magnetic field (Lazarian 2020).

2.2 Bayesian Analysis

We apply a Bayesian approach to analyse our data and estimate the model parameters. We use a Markov Chain Monte Carlo (MCMC) algorithm (emcee package Foreman-Mackey et al. 2013) to draw samples that approximate the posterior distribution, and use these for inference. In Bayesian analysis, the choice of the prior is important and can affect the results. In Appendix A2 we run a series of prior sensitivity tests to determine what effect each prior choice has on the resulting posterior distribution. We find the observation data is best described by a Gaussian distribution for α_2 , B_0 , n_0 and $\ln V$ and a flat PDF for α_1 .

For the numerical data we use a broad and flat PDF for all parameters due to the range of simulations and the spread of data in each. A detailed discussion of our choice can be found in Appendix A2.

The observational data sets that we use include both Zeeman and DCF measurements. This requires that we must apply two different likelihood functions, because of the differences in how the errors are treated for these different measurement techniques. For the DCF data we use a Gaussian likelihood function as the errors are symmetrical in the plane-of-sky. The Zeeman data are a little more complex due to being line-of-sight. For this data set we use a folded normal distribution on the absolute values to avoid getting negative error values in the magnetic field strength. The equations and application are described in detail in Appendices A1 and A3. The Crutcher et al. (2010) fit was to the maximum B in order to overcome the known issue of the under-prediction of B from only taking one component of the B-field vector. They used a flat PDF for the priors, which has subsequently been used in following studies (Jiang et al. 2020).

For the observational results we run the MCMC using the Crutcher result as the initial parameter space for each data set and setting $\ln V$ to 0.5, which is large enough to show distrust in the errors but small enough that they are not wildly inaccurate. We use 100 walkers (starting parameters) randomly sampled around the Crutcher result to determine the starting positions for the MCMC to begin its analysis, and 25,000 steps, discarding the first 5,000 steps and thinning to every twentieth step. This ensures convergence of the fit and avoidance of auto-correlation. These are the results presented in Section 3.

We use the same choices for the numerical simulations with only a slight variation in the initial parameters used and number of steps. For these data, we find that the MCMC converges on all five parameters relatively quickly. We therefore only run for 5,000 steps, discarding the first 1,000 and thinning to every fifteenth step. The differences are discussed in more detail in Appendix A5.

For both the observational and numerical simulation results we report the median (best-fitting relation computed from MCMC) of the MCMC posterior samples for each parameter instead of the mode. Whilst the mode is the value with the highest posterior density, the median is more representative of the typical parameter values and represents a more general model.

2.3 DCF errors

When B_{pos} is inferred from the DCF method, the main uncertainties come from the following sources:

(i) Density uncertainty: The estimate of the density in Eq. (1) is usually obtained from the thermal dust emission that allows us to estimate the mass, and from the assumption of a specific geometry. To estimate the mass, a certain dust temperature and a dust opacity at the observing frequency is usually assumed. These two quantities are highly uncertain, with the dust opacity varying by a factor of 2–4 (e.g., Ossenkopf & Henning 1994; Li et al. 2024).

(ii) Velocity dispersion uncertainty: The velocity dispersion is measured from a molecular gas tracer. It is typically assumed that the entire velocity dispersion, which is usually dominated by non-thermal motions, is due to turbulence only. Therefore, the uncertainty comes from the specific properties of the tracer used, and from the fact that a non-negligible part of the velocity dispersion might be due to bulk, non-turbulent, motions. If this is not taken into account, the magnetic field can be overestimated by a factor of 2, as shown in Palau et al. (2021).

(iii) Dispersion in polarization position angles uncertainty: When a number of polarization segments have been detected in a specific region, σ_{PA} can be measured in different ways, such as the standard deviation of the position angles, Gaussian fitting to the position angles histograms, or more sophisticated approaches based on the structure function such as those proposed by Hildebrand et al. (2009) or Houde et al. (2009). These different approaches to estimate σ_{PA} typically differ by a factor of 2 (e.g., Palau et al. 2021).

(iv) f factor uncertainty: The correction factor f has been proposed to correct for several biases, such as projection effects along the line of sight, the fact that the magnetic field is averaged out within the beam, that only one of the three velocity components is used, or that there is no exact equipartition between the magnetic energy of the perturbed magnetic field and the kinetic energy. This factor has been estimated from numerical simulations, and it is around 0.5, although it can reach lower values of around 0.2 (e.g., Heitsch et al. 2001; Ostriker et al. 2001; Liu et al. 2022).

(v) Sparse sampling effects: Due to sensitivity limitations, only a fraction of the total area emitting polarized radiation is detected, restricting the reliability of the measurement. An extreme case is where very few polarization segments are detected, suggesting a relatively uniform and strong field, while deeper observations reveal an underlying more turbulent field. The relative uncertainty due to sparse sampling can reach up to 60% (Palau et al. 2021). This uncertainty is explained in detail in Liu et al. (2019).

In addition to the aforementioned uncertainties, the choice of the DCF or the ST method for interpretation of the polarization data can introduce additional biases. The main dif-

ference between the DCF and ST methods is the dependence on σ_{PA} (apart from the $\sqrt{2}$ factor): in the DCF method, $B_{\text{pos}} \propto 1/\sigma_{\text{PA}}$, while in the ST method, $B_{\text{pos}} \propto 1/\sqrt{\sigma_{\text{PA}}}$. Since in most cases $\sigma_{\text{PA}} < 1$ rad, the ST method results in B_{pos} systematically smaller by a factor of 2–4 compared to the values obtained with the DCF method. In order to showcase the difference between both methods, our dataset includes the same sample of Palau et al. (2021) with the resulting B_{pos} obtained from DCF (column 6 of Table 5 of Palau et al. 2021), and from ST (column 8 of Table A1 of Camacho et al. 2023).

Taking into account the combination of all the potential uncertainties associated with the B_{pos} measurements, the global uncertainties could reach up to a factor of ~ 10 . Further details on the uncertainties associated with magnetic field measurements can be found in the recent reviews by Liu et al. (2021), Liu et al. (2022, see their Sec. 2.2), and Pattle et al. (2022).

2.4 Observational data sets

The Zeeman splitting data of Crutcher et al. (2010, Table 1), used for their analysis, provide estimates of the line-of-sight component of the magnetic field. On the other hand, observations of polarized thermal dust emission provide estimates of the plane-of-sky magnetic field strength. For this work we used the compilation of Pattle et al. (2022), along with the two different analyses of the polarization data taken by Palau et al. (2021), mentioned in the previous section.

The data is split into ten different sets in order to provide a broad and statistically significant analysis. This consists of four (non-scaled) data sets that represent the original Zeeman data along with three new data sets based on the DCF measurements from Pattle et al. (2022). These are:

1 Zeeman: The Zeeman data from Crutcher et al. (2010).

2 DCF_{sym}: The DCF data from Pattle et al. (2022) with only symmetric errors.

3 DCF_{asym}: The DCF data from Pattle et al. (2022) that has symmetric and asymmetric errors, the latter of which are treated as symmetric.

4 DCF_{kde} - As DCF_{asym} plus errors computed using a kernel density estimate (KDE) on data from Pattle et al. (2022) that did not include errors.

The remaining six sets use the same basic data as the first four with data scaled to represent a 3D derived field strength based upon a scale factor for the DCF data (Crutcher 2004)

$$|\mathbf{B}| = \frac{4}{\pi} B_{\text{pos}}, \quad (3)$$

and one for the Zeeman data (Crutcher et al. 2004),

$$|\mathbf{B}| = 2B_z. \quad (4)$$

Pattle et al. (2022) show that the average DCF measurement is a factor $c = 6.3 \pm 1.5$ higher than the average Zeeman measurement. This is a different conversion factor to f already seen in Equation 1 which is applied to the raw data, as c is specifically the ratio between the DCF and Zeeman data. We perform a fit with this discrepancy taken into account where we reduce only the DCF measurements by this factor c . We do not scale the errors as they are likely understated, since the DCF over predicts the field strength. No reduction

in the errors also allows for variability in the scale factor. A further data set including this factor is defined. Our Fiducial data set includes both Zeeman and scaled DCF data sets.

The six 3D scaled data sets are:

5 3D-Zeeman: The Zeeman data from [Crutcher et al. \(2010\)](#).

6 3D-DCF_{sym}: The DCF data from [Pattle et al. \(2022\)](#) that only has symmetric errors.

7 3D-DCF_{asym}: The DCF data from [Pattle et al. \(2022\)](#) that has symmetric and asymmetric errors.

8 3D-DCF_{kde}: As DCF_{asym} plus KDE errors applied to data from [Pattle et al. \(2022\)](#) that did not include errors.

9 Scaled: 3D-DCF_{sym} scaled down by a factor of 6.3

10 Fiducial: 3D-Zeeman and 3D-DCF_{sym} data sets combined but with 3D-DCF_{sym} scaled down by a factor of 6.3

We tested whether unrealistically high precision in some of the errors was biasing the results. To do this we set any error that is smaller than 15% to 15%. We saw no significant change in the results, and so do not include this analysis.

2.5 Numerical simulations: methods and data sets

We perform the Bayesian MCMC analysis on 19 numerical simulations that cover a wide range of initial conditions, densities, magnetic fields strengths and scales. The systems covered in our set of simulations range from full Milky Way-like galaxies to protoplanetary discs. The simulations themselves were executed with a variety of codes including AREPO ([Springel 2010](#)), FLASH ([Fryxell et al. 2000](#)), RAMSES ([Teyssier 2002](#)), and PENCIL ([Brandenburg & Dobler 2002; Brandenburg et al. 2020](#)).

These codes use different types of meshes and refinement criteria. AREPO solves the MHD equations on a Voronoi moving mesh refined to increase mass resolution in high density regions. FLASH and RAMSES are adaptive mesh refinement (AMR) codes that use Cartesian grids to define cells. PENCIL is a high-order single-grid code using sixth-order space and fourth-order time derivatives. For a more detailed description of each code we refer the reader to the cited method papers. For each simulation presented here we refer to the original work for a detailed discussion of their numerical setup. The high-resolution simulations of dwarf galaxies presented here are novel and have been run specifically for this work, so we provide a summary of the key differences to the original simulations in Appendix B.

Each simulation used in this analysis has millions to billions of data points. To run the MCMC on such large data sets is computationally expensive and time consuming. In order to reduce the resource usage we take 10 random samples of 50,000 points from each simulation. So instead of completing one MCMC on billions of points for one simulation, we run it 10 times on a total of 500,000 data points. See Appendix A5) for a more detailed explanation.

For each simulation we plot the volume weighted magnetic field magnitude $|\mathbf{B}|$ in each computational cell against the number density n of the cell and overlay the original relation of [Crutcher et al. \(2010\)](#). The volume weighted average fit to the data is calculated by binning the data into 500 equally sized log spaced density bins and then calculating the volume weighted average of each bin. This is done to compare the

MCMC analysis run on a much smaller data set to the full data.

We volume weight the magnetic field in the grid codes as this is most comparable to the Eulerian nature of the codes. For the AREPO simulations we volume weight due to oversampling in the densest regions. The mesh is non-uniform and so a grid average would be biased towards the densest regions. By volume weighting we again take an Eulerian point of view meaning that we get the typical view at a randomly chosen point in space.

3 OBSERVATIONAL RESULTS

3.1 Fits to the observational data

The main result from the observational data is shown in Figure 1. This shows a generalised form of the relationship based on the combination of Zeeman data from [Crutcher et al. \(2010\)](#) and scaled DCF from [Pattle et al. \(2022\)](#) of magnetic field strength as a function of number density, our Fiducial data set (10).

For each MCMC model run we determine the posterior distribution for each parameter as shown in Figure 2. This figure shows the probability density distribution of the relationships between each parameter giving us a visual representation of the scatter in the data. Each point represents one of the results from the 45,000 steps in the MCMC. We also show the results from the original fit of [Crutcher et al. \(2010\)](#).

Figures 3 and 5 show the MCMC best fits to different observational data sub-sets plotted using the techniques described below against the data and original relationship. Tables 1 and 2 show the results with the 68% credible interval for each parameter and Figure 4 shows the table results in a graphical form for ease of comparison. The data in the top plots of each Figure are the original Zeeman data from [Crutcher et al. \(2010\)](#). In the bottom plot the data are taken from Figure 2b of [Pattle et al. \(2022\)](#), coloured to represent different treatments of the errors, and including DCF data from [Palau et al. \(2021\)](#) and the ST method data from [Camacho et al. \(2023\)](#).

3.2 Non-scaled results

For the individual observational data sets we first analysed the data as presented in their original publications using data sets 1 to 4. Table 1 shows the best-fitting relation computed from the MCMC and its 68% credible interval computed from the posterior distribution for each parameter for each data set. We also include the values for $\ln V$, a nuisance factor that describes the intrinsic variation on the errors, described in more detail in Appendix A1. Figure 3 shows the models corresponding to the best-fitting parameter values computed from MCMC plotted against the data and original relationships. We also plot models constructed using 100 posterior samples of the MCMC to show the variance in the fits.

The exponent in the low density regime, α_1 , is greater than zero in all cases and is consistent across all data sets. It is smaller than the expectation for either the kinematically or the dynamically collapsing cases. The transition density between the regimes and the field strength normalisation is uncertain, and varies between datasets. In the high density

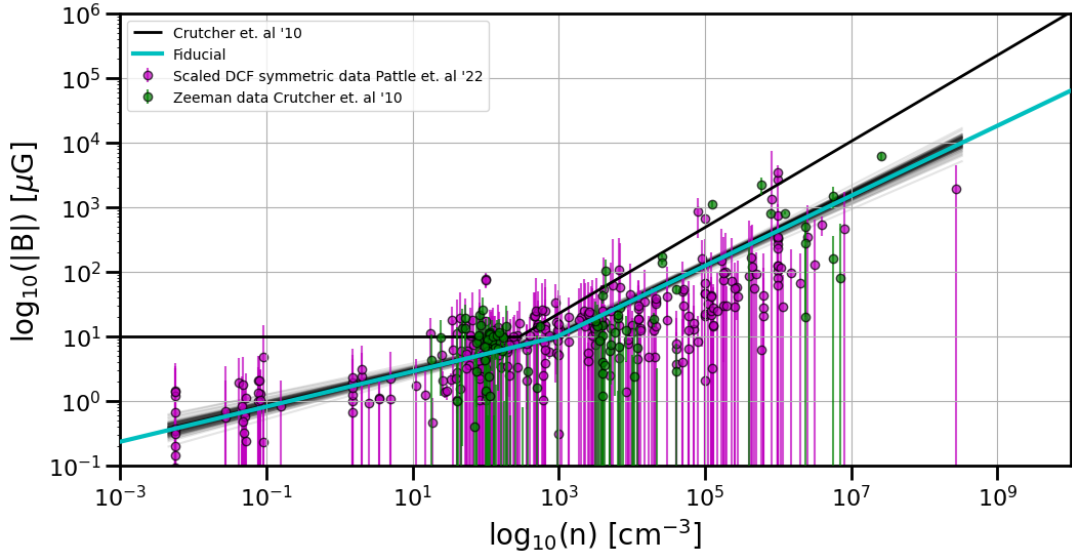


Figure 1. A general fit to the observed magnetic field strength as a function of number density based on Zeeman data from Crutcher et al. (2010) and scaled DCF data from Pattle et al. (2022) combined in our Fiducial data set. The cyan line is the best central estimate of the median result from our Bayesian analysis of that data set. The grey lines on each plot are models computed for 100 posterior parameter samples from our MCMC computation. We see that the combined data set shows exponents: $\alpha_1 = 0.27 \pm 0.017$ and $\alpha_2 = 0.54 \pm 0.018$ with $n_0 = 924_{-144}^{+145}$.

regime the exponent, α_2 , is closer to the dynamic value (0.5) than the kinematic exponent (0.67), with the exception of the Zeeman data set. The data set that includes the KDE errors has a value lower than the dynamic case and both α_1 and α_2 suggest a single power-law or possibly a three part power-law with a break at higher densities. We discuss this more in Section 5.2.

A limitation of our analysis is that the errors in the underlying data sets are mostly broad estimates and some data lack errors completely. The lack of errors particularly affects the densest gas ($n > 10^6 \text{ cm}^{-3}$) where Pattle et al. (2022) suggested there could be a turn over and flattening of the relationship.

3.3 Scaled results

We next consider the results for the six 3D scaled data sets 5 to 10. Table 2 shows the best-fitting parameters for the 3D scaled data sets including the Scaled and Fiducial data sets with the 68% credible interval on each parameter. Again we include $\ln V$ to describe the intrinsic variation in the errors. Figure 5 shows these results plotted against the data and original relation (black line). Again we also show 100 posterior samples from the MCMC (grey lines), to show the variance in fit.

As with the non-scaled results, α_1 is again greater than zero in all data sets and consistent across all data sets at ~ 0.27 with only 3D-DCF_{kde} (8) showing variation. Data sets 5, 6, 7 and 8 show very little variation from their non-scaled counter parts. The result for the Scaled data set, 9, is similar to the Fiducial data set, 10. Both show variation from the original relation with a positive exponent in the diffuse gas, though lower than the expectation for either the kinematically or dynamically collapsing cases, and a value of α_2 that lies closer to the dynamic exponent 0.5 than the kinematic value of 0.67

in both data sets. In summary, our analysis of the observational data shows that the B - n relation in the diffuse gas has an exponent of $\alpha_1 = 0.24 \pm 0.017$ and $n_0 = 924_{-144}^{+145} \text{ cm}^{-3}$.

4 NUMERICAL SIMULATION RESULTS

In this section we use the same statistical approach to deduce the B - n relation that arises in a heterogeneous set of numerical simulations using different codes, scales, and approximations as described in Section 2.5. Because the numerical simulations span a much larger range of n than the observational data, we relax our prior distributions to reflect the lack of knowledge that we have in this regime. Thus, we use flat priors as defined in Appendix A2 for this portion of the analysis.

We show in Table 3 the median best-fitting parameter values for each of the 19 numerical simulations examined in this work. The median is taken from the 10 MCMC fits completed for each simulation and errors are propagated through. For a detailed description of each simulation see the corresponding section below.

Examining the results we find large variations in all free parameters across the simulations, for example by up to a factor of nearly 100,000 in n_0 from a minimum of 0.06 cm^{-3} to a maximum of 5666.70 cm^{-3} . Although no simulation completely matches the observational relation, MHD_SAT_HR agrees well in the exponents and transition field strength, differing only in the break density. The exponent of the diffuse gas for each simulation, α_1 , varies from -0.28 in IMHD to 0.83 in MHD_10_LR. Most simulations that trace the dense gas well show an α_2 of ~ 0.5 or greater. The exceptions are the simulations run for shorter time scales like B3, B6, KPC_LOW, KPC_HIGH, SSD_35 and SSD_98.

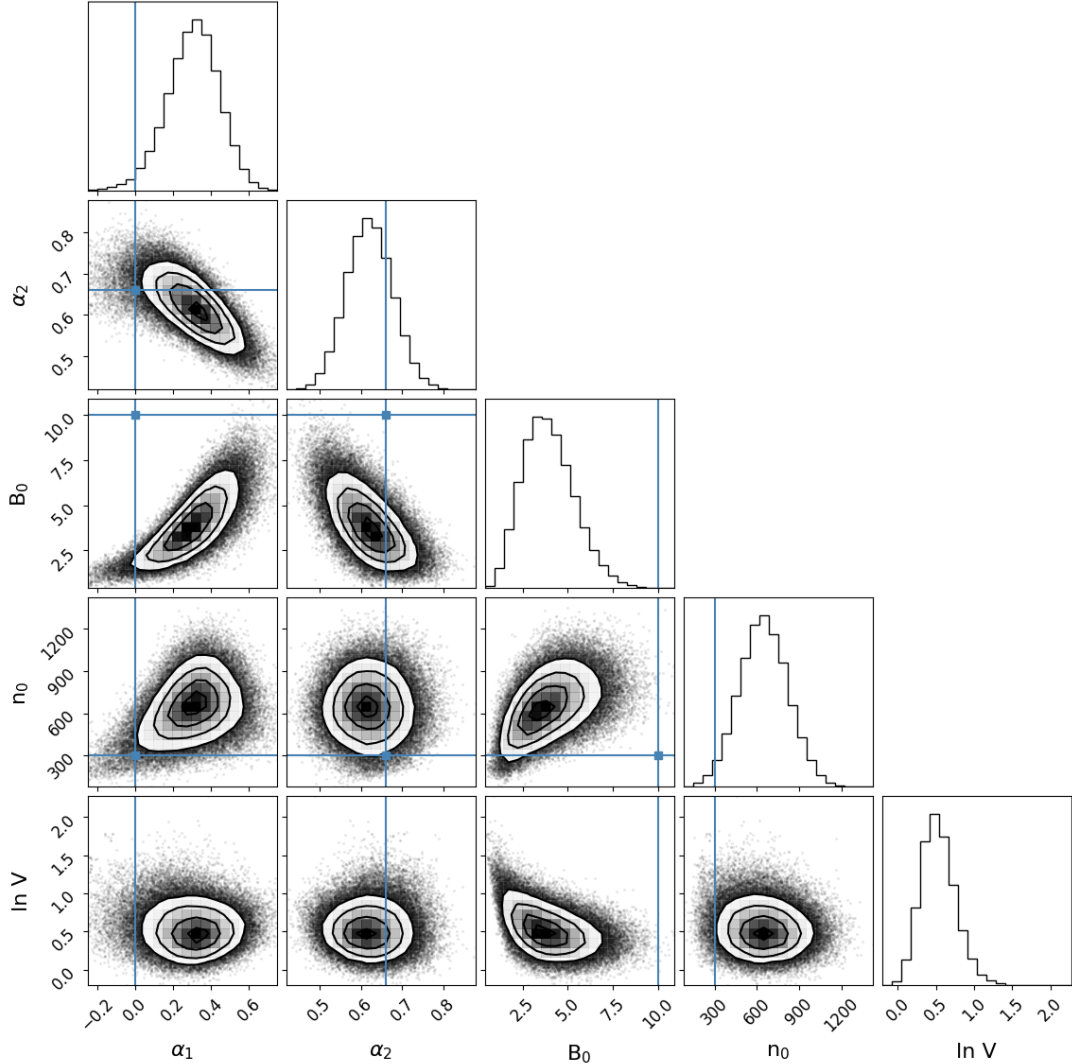


Figure 2. Posterior distributions produced by the MCMC routine for data set 1. We can see the correlations between parameters and note that for this data set the distributions are unimodal with well-constrained best-fitting values. The histograms show Gaussian-like distributions for each parameter. The blue lines show the relations found by Crutcher et al. (2010), showing how our results have deviated.

Data set	α_1	α_2	n_0 (cm^{-3})	B_0 (μG)	$\ln V$
1) Zeeman	$0.307^{+0.129}_{-0.141}$	$0.619^{+0.057}_{-0.055}$	$643.972^{+172.803}_{-169.214}$	$3.813^{+1.551}_{-1.299}$	$0.511^{+0.239}_{-0.206}$
2) DCF _{sym}	$0.262^{+0.018}_{-0.018}$	$0.528^{+0.018}_{-0.018}$	$946.254^{+140.406}_{-142.352}$	$45.160^{+4.186}_{-3.991}$	$0.397^{+0.090}_{-0.085}$
3) DCF _{asym}	$0.259^{+0.018}_{-0.018}$	$0.520^{+0.018}_{-0.017}$	$958.571^{+140.461}_{-141.857}$	$44.806^{+4.065}_{-3.903}$	$0.392^{+0.088}_{-0.083}$
4) DCF _{kde}	$0.294^{+0.015}_{-0.016}$	$0.411^{+0.011}_{-0.011}$	$529.378^{+138.722}_{-129.501}$	$49.425^{+4.492}_{-4.529}$	$0.226^{+0.058}_{-0.055}$

Table 1. The best-fitting parameters for the observational B - n relation computed from MCMC along with the 68% credible interval for each parameter from the MCMC posterior samples provided by the Bayesian analysis. We note that the model that includes the KDE derived errors does not reach convergence for n_0 and B_0 . [MM: should this perhaps be discussed in the text rather than just the caption?] We can see that by deriving a relationship from a broader density range covered by DCF measurements the dense gas relationship has a smaller exponent than predicted by the Zeeman data alone and that the diffuse gas has a positive power-law index.

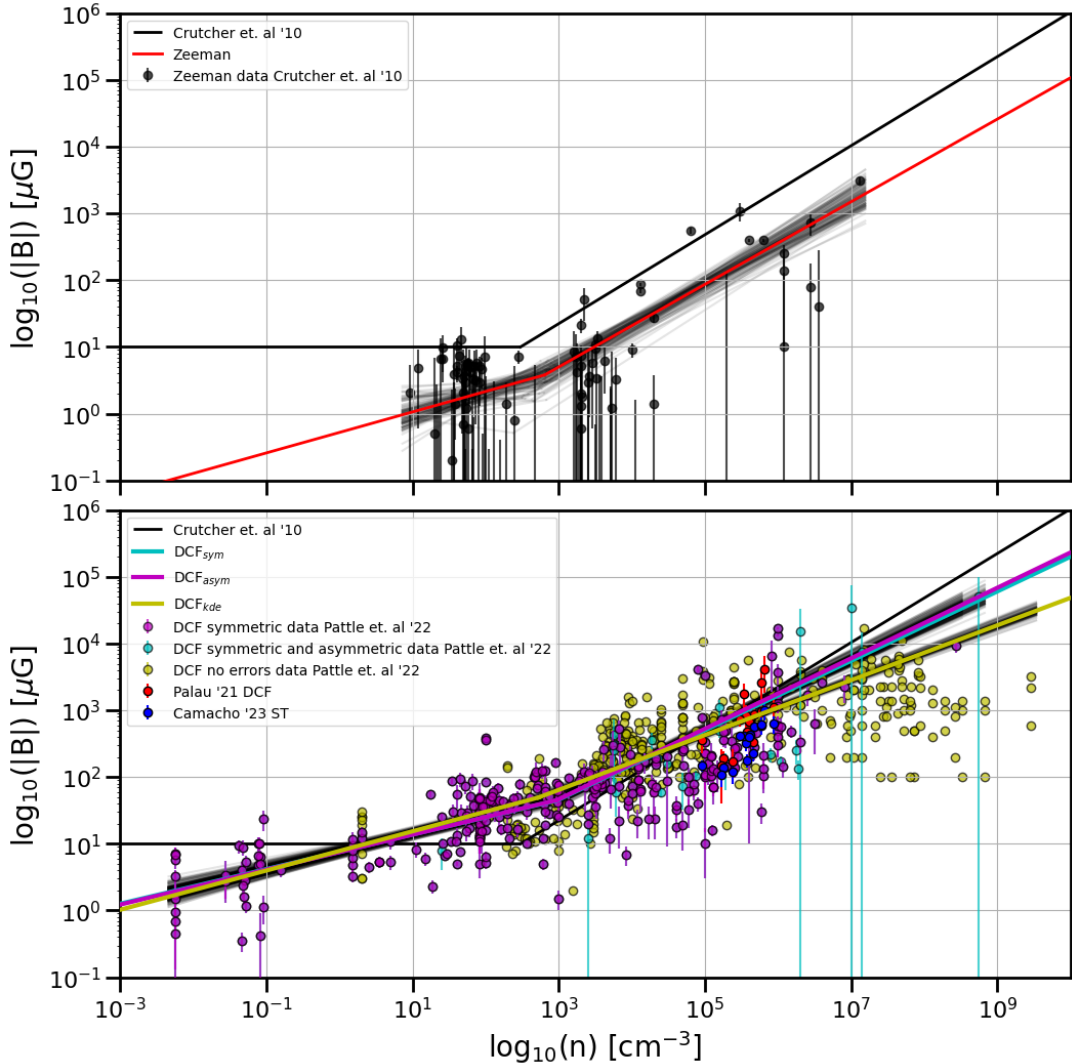


Figure 3. Fits to observations of magnetic field strength as a function of number density. Top: Zeeman data from Crutcher et al. (2010). The red line is the best central estimate of the median result from our Bayesian analysis. We can see that the diffuse region is not well constrained. Bottom: DCF data from Pattle et al. (2022) with symmetric errors (magenta points), data with symmetric and asymmetric errors (cyan points), data without errors (yellow points), data from Palau et al. (2021) (red points), and ST analyses from Camacho et al. (2023) of the data from Palau et al. (2021), shown as blue points. The solid black line on both plots is the relationship proposed by Crutcher et al. (2010). The coloured lines show the models corresponding to the median parameter values for each data set. The grey lines on each plot are models computed for 100 posterior parameter samples from our MCMC analysis.

4.1 Core collapse simulations

The data presented in Figure 6 are from simulations of molecular cloud cores collapsing to form protoplanetary discs and envelopes, using the AMR code RAMSES in either the ideal MHD limit, or including non-ideal resistivities (Lebreuilly et al. 2021). The resolution of these simulations goes from 0.012 pc (2460 au) in the most diffuse gas to 5.84×10^{-6} pc (1.2 au) in the densest gas. A uniform seed field of $\sim 9.4 \times 10^{-5}$ G is initialised in the core. For more detail we refer to the original publication. This simulation includes higher density gas characteristic of protostellar discs than is possible to measure in the observed systems. There appears to be a well-defined B - n relation with a best-fitting power-law index of $\alpha_2 \sim 1/2$. α_1 has a negative value as the simulations only include small amounts of lower density gas

in outflow cavities unrepresentative of the ISM. We see that the fits of the two simulations are very similar. This is because ambipolar diffusion, that can diffuse magnetic fields, only becomes significant at very high densities ($n > 10^9$ cm $^{-3}$). Above those densities, we note that the B - n relation has a plateau for the NI simulation. This plateau is well documented (Masson et al. 2016; Vaytet et al. 2018; Hennebelle et al. 2020; Commerçon et al. 2022).

4.2 Turbulent box simulations

In this subsection we present results from stratified, horizontally periodic domains with and without galactic shear. Each simulation includes supernova (SN) driving and a disk gravitational potential. All bar the simulations of Gent et al. (2021) and Gent et al. (2024) include self-gravity. For a more

Data set	α_1	α_2	n_0 (cm $^{-3}$)	B_0 (μ G)	$\ln V$
5) 3D-Zeeman	$0.273^{+0.100}_{-0.103}$	$0.631^{+0.049}_{-0.047}$	$622.200^{+158.181}_{-148.106}$	$6.818^{+1.487}_{-1.437}$	$0.532^{+0.220}_{-0.199}$
6) 3D-DCF _{sym}	$0.262^{+0.018}_{-0.018}$	$0.529^{+0.018}_{-0.018}$	$910.992^{+125.756}_{-128.815}$	$57.780^{+5.005}_{-4.862}$	$0.380^{+0.087}_{-0.082}$
7) 3D-DCF _{asym}	$0.260^{+0.017}_{-0.018}$	$0.521^{+0.017}_{-0.017}$	$923.291^{+125.824}_{-129.547}$	$57.227^{+4.892}_{-4.723}$	$0.377^{+0.084}_{-0.080}$
8) 3D-DCF _{kde}	$0.292^{+0.015}_{-0.016}$	$0.414^{+0.011}_{-0.011}$	$556.539^{+124.796}_{-118.019}$	$63.370^{+5.117}_{-5.123}$	$0.223^{+0.057}_{-0.055}$
9) Scaled	$0.279^{+0.018}_{-0.018}$	$0.506^{+0.019}_{-0.018}$	$833.824^{+153.431}_{-144.747}$	$10.222^{+0.907}_{-0.881}$	$0.225^{+0.090}_{-0.083}$
10) Fiducial	$0.272^{+0.017}_{-0.017}$	$0.542^{+0.018}_{-0.018}$	$923.525^{+144.870}_{-144.370}$	$9.685^{+0.848}_{-0.816}$	$0.357^{+0.087}_{-0.081}$

Table 2. The best fits to the B - n parameters in the observational data, converted to 3D using the method suggested by Crutcher (2004) and Crutcher et al. (2004). We note that the results are similar to the non-scaled data in Table 1. The final row shows the best-fitting parameters for our Fiducial combined 3D data set of the Zeeman data and DCF data to provide our best version of the relationship. A graphical representation can be seen in Figure 4.

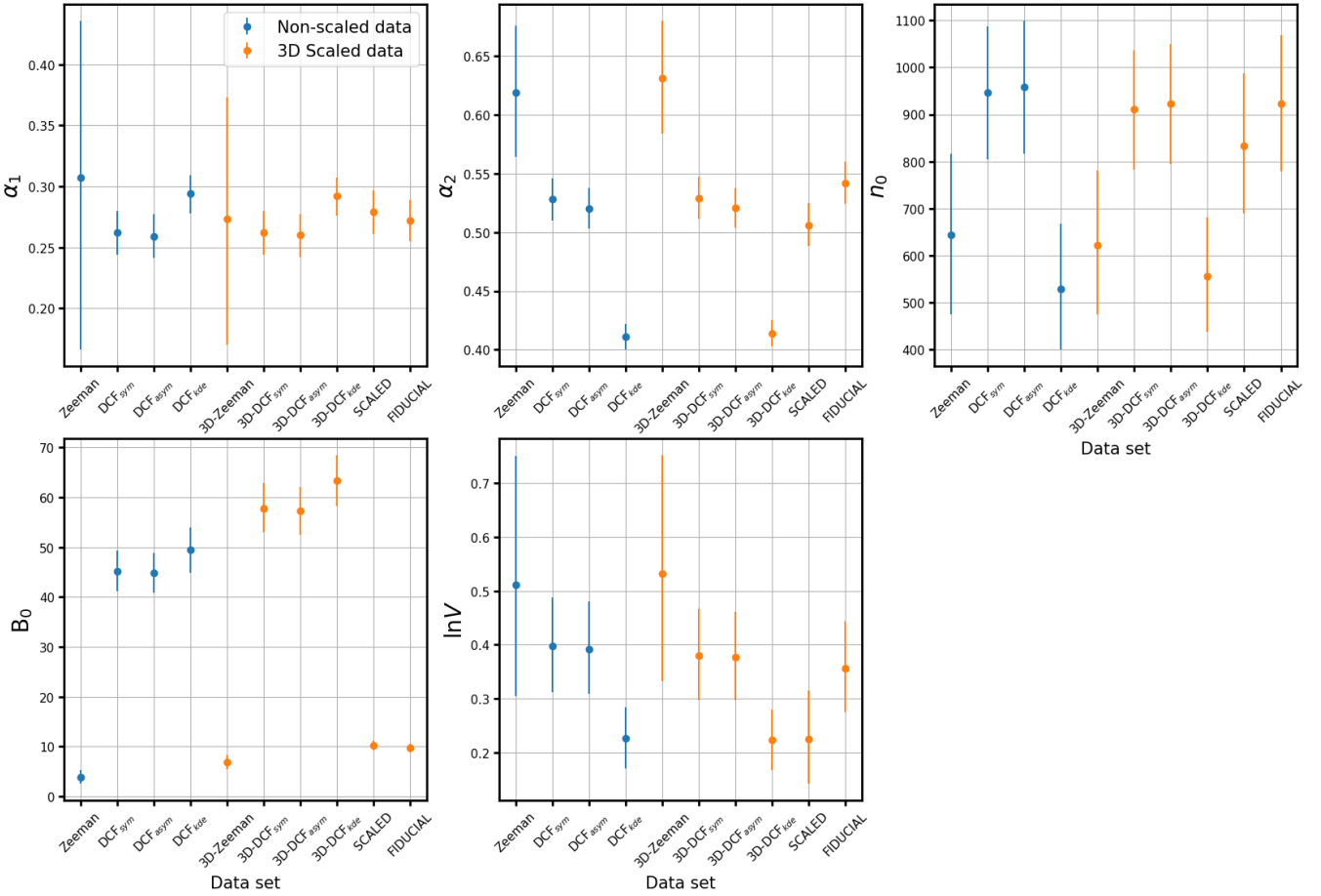


Figure 4. A graphical representation of the observational B - n parameters presented in Tables 1 and 2. The blue points are the data sets as originally published, while the orange points are 3D converted or scaled data. We can clearly see how similar α_1 is across the data sets. The Scaled and Fiducial results are within each others 68% credibility intervals.

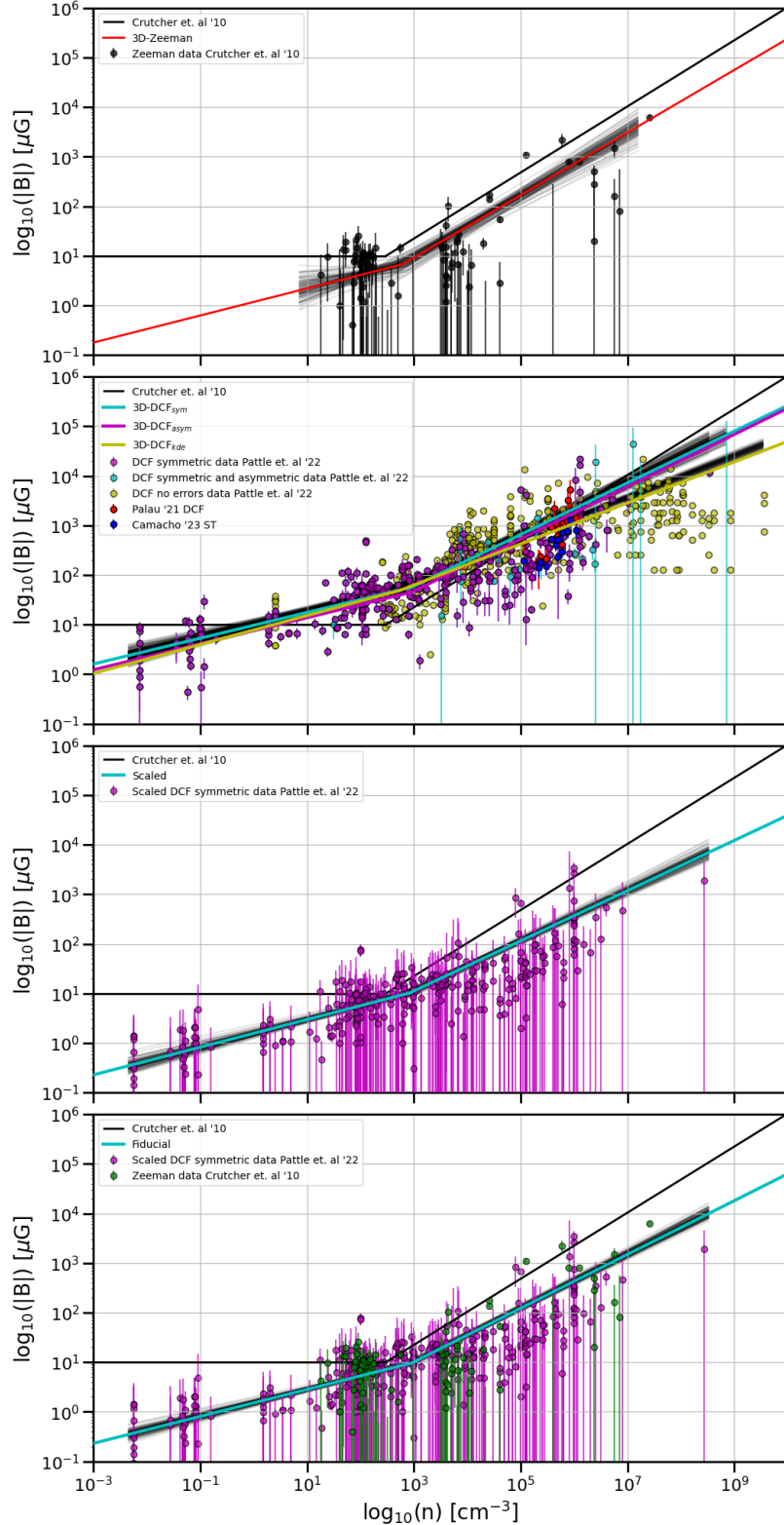


Figure 5. The top two plots are the same as Figure 3 but adjusted for 3D. The bottom two plots show the MCMC median results for data sets Scaled (9) and Fiducial (10). In the bottom two plots the DCF data match the other plots and the (green points) show the Zeeman data. All the data in these plots are scaled to represent the three-dimensional (3D) field strengths using the conversion factors from Equations 3 and 4. The bottom plot has the DCF scaled down by a factor of 6.3 to be inline with the Zeeman data, as explained by Pattle et al. (2022).

Simulation	α_1	α_2	n_0 (cm $^{-3}$)	B_0 (μ G)	$\ln V$	Section	Reference
1) NI	-0.20 $^{+0.02}_{-0.02}$	0.56 $^{+0.00}_{-0.00}$	705.79 $^{+48.8}_{-40.1}$	14.39 $^{+0.24}_{-0.25}$	-0.17 $^{-0.02}_{+0.02}$	4.1	Lebreuilly et al. (2021)
2) IMHD	-0.28 $^{+0.02}_{-0.02}$	0.56 $^{+0.00}_{-0.00}$	705.48 $^{+37.19}_{-82.17}$	13.78 $^{+0.21}_{-0.21}$	-0.24 $^{+0.02}_{-0.02}$	4.1	Lebreuilly et al. (2021)
3) B3	0.58 $^{+0.00}_{-0.00}$	0.21 $^{+0.00}_{-0.00}$	0.39 $^{+0.03}_{-0.03}$	1.72 $^{+0.05}_{-0.05}$	-0.16 $^{+0.02}_{-0.02}$	4.2	Girichidis et al. (2018)
4) B6	0.69 $^{+0.00}_{-0.00}$	0.17 $^{+0.00}_{-0.00}$	0.20 $^{+0.02}_{-0.02}$	1.88 $^{+0.03}_{-0.03}$	-0.26 $^{+0.02}_{-0.02}$	4.2	Girichidis et al. (2018)
5) KPC_LOW	0.12 $^{+0.02}_{-0.02}$	0.16 $^{+0.02}_{-0.02}$	1.02 $^{+356.0}_{-0.02}$	3.06 $^{+0.03}_{-0.03}$	-0.53 $^{+0.02}_{-0.02}$	4.2	Brucy et al. (2023)
6) KPC_HIGH	0.23 $^{+0.00}_{-0.00}$	0.13 $^{+0.02}_{-0.02}$	19.58 $^{+12.31}_{-3.83}$	10.64 $^{+0.45}_{-0.39}$	-0.49 $^{+0.02}_{-0.02}$	4.2	Colman et al. (2022)
7) SSD_35	-0.03 $^{+0.00}_{-0.00}$	-0.61 $^{+0.02}_{-0.02}$	0.08 $^{+0.00}_{-0.00}$	0.11 $^{+0.00}_{-0.00}$	0.01 $^{+0.02}_{-0.02}$	4.2	Gent et al. (2021)
8) SSD_98	0.45 $^{+0.00}_{-0.00}$	-0.07 $^{+0.02}_{-0.02}$	0.06 $^{+0.00}_{-0.00}$	0.21 $^{+0.00}_{-0.00}$	-0.01 $^{+0.02}_{-0.02}$	4.2	Gent et al. (2021)
9) SSD_700	0.40 $^{+0.00}_{-0.00}$	0.19 $^{+0.02}_{-0.02}$	0.24 $^{+0.10}_{-0.03}$	1.15 $^{+0.24}_{-0.05}$	-0.18 $^{+0.02}_{-0.02}$	4.2	Gent et al. (2021)
10) LSD_3500	0.53 $^{+0.00}_{-0.00}$	0.17 $^{+0.02}_{-0.02}$	0.16 $^{+0.02}_{-0.02}$	9.10 $^{+0.25}_{-0.25}$	-0.62 $^{+0.02}_{-0.02}$	4.2	Gent et al. (2024)
11) MHD_10	0.49 $^{+0.00}_{-0.00}$	0.45 $^{+0.02}_{-0.02}$	355.27 $^{+29.36}_{-5.16}$	11.27 $^{+0.46}_{-0.34}$	-0.50 $^{+0.02}_{-0.02}$	4.3.1	Whitworth et al. (2023)
12) MHD_SAT	0.36 $^{+0.00}_{-0.00}$	0.91 $^{+0.08}_{-0.08}$	5666.70 $^{+650.68}_{-1004.13}$	34.57 $^{+2.53}_{-1.80}$	-0.61 $^{+0.02}_{-0.02}$	4.3.1	Whitworth et al. (2023)
13) MHD_10_HR	0.46 $^{+0.00}_{-0.00}$	0.49 $^{+0.02}_{-0.02}$	1459.84 $^{+324.80}_{-400.85}$	25.68 $^{+4.80}_{-4.04}$	-0.54 $^{+0.02}_{-0.02}$	4.3.1	New simulation
14) MHD_SAT_HR	0.28 $^{+0.00}_{-0.00}$	0.55 $^{+0.02}_{-0.02}$	248.86 $^{+13.03}_{-18.41}$	7.61 $^{+0.06}_{-0.02}$	-0.44 $^{+0.02}_{-0.02}$	4.3.1	New simulation
15) MHD_10_LR	0.8 $^{+0.02}_{-0.02}$	0.52 $^{+0.02}_{-0.02}$	0.52 $^{+0.02}_{-0.02}$	0.08 $^{+0.00}_{-0.00}$	-0.16 $^{+0.02}_{-0.02}$	4.3.1	Whitworth et al. (2023)
16) MW_RAM_1	0.59 $^{+0.00}_{-0.00}$	0.43 $^{+0.02}_{-0.02}$	3.17 $^{+0.00}_{-0.07}$	16.91 $^{+0.22}_{-0.02}$	-0.58 $^{+0.02}_{-0.02}$	4.3.2	Robinson & Wadsley (2023)
17) MW_RAM_2	0.81 $^{+0.02}_{-0.02}$	0.51 $^{+0.00}_{-0.00}$	0.06 $^{+0.01}_{-0.01}$	0.45 $^{+0.03}_{-0.03}$	-0.18 $^{+0.02}_{-0.02}$	4.3.2	Robinson & Wadsley (2023)
18) MWR_R1	0.79 $^{+0.02}_{-0.02}$	0.50 $^{+0.00}_{-0.00}$	0.64 $^{+0.07}_{-0.06}$	1.77 $^{+0.12}_{-0.08}$	-0.40 $^{+0.02}_{-0.02}$	4.3.2	Zhao et al. (2024)
19) MWR_R2	0.72 $^{+0.02}_{-0.02}$	0.47 $^{+0.00}_{-0.00}$	0.70 $^{+0.08}_{-0.08}$	1.72 $^{+0.09}_{-0.09}$	-0.31 $^{+0.02}_{-0.02}$	4.3.2	Zhao et al. (2024)

Table 3. The best-fitting parameters in the B - n relation computed from MCMC from fits to random samples from the numerical simulation data, and the corresponding section where we discuss the results. Errors have been propagated from the 68% credible intervals on the 10 MCMC fits we perform for each simulation. Where we see large errors on small values, this arises from outliers due to our random sampling of the data sets. We note the small errors on the exponents α_1 and α_2 showing that they are well constrained for each simulation. It is clear from these results that the relationship changes dramatically across simulations, with large variations in all free parameters.

detailed discussion on the initial conditions of each simulation we point the reader to the original publications.

The results from two $(0.5 \text{ kpc})^3$ stratified box simulations taken from the SILCC simulations of Girichidis et al. (2018) with the FLASH AMR code are shown in Figure 7. We show two simulations, B3 and B6, run with initial seed fields of $3 \mu\text{G}$ and $6 \mu\text{G}$, respectively. Both simulations have a base spatial resolution of 4 pc, going down to 1 pc in the densest gas, and have been run for 60 Myr.

Comparing the two simulations, we find that $n_0 \leq 0.4 \text{ cm}^{-3}$ and that they have a diffuse gas exponent of $\alpha_1 = 0.58$ – 0.69 . In the dense gas the exponent is reduced; $\alpha_2 = 0.21$ in B3 and $\alpha_2 = 0.17$ in B6 in contrast to the Crutcher et al. (2010) relationship.

The results shown in Figure 8 are taken from Colman et al.

(2022) and Brucy et al. (2023). They used the AMR code RAMSES to compute MHD simulations in a $(1 \text{ kpc})^3$ domain. The two simulations shown include one with a uniform cell resolution of 4 pc and another with an AMR grid ranging from 4 pc in the low density gas to 0.12 pc in the high density. The lower and uniform resolution simulation KPC_LOW was run for 58 Myr while the AMR simulation KPC_HIGH was run for an additional 30 Myr at uniform resolution before being allowed to refine to higher resolution and run for an additional 20 Myr. The initial magnetic field in both simulations was set to $7 \mu\text{G}$.

The exponents in both the dense and diffuse gas of KPC_LOW are small, $\alpha_1 = 0.12$ and $\alpha_2 = 0.16$. In KPC_HIGH the diffuse gas exponent is larger, $\alpha_1 = 0.23$, whilst the dense gas exponent remains almost the same,

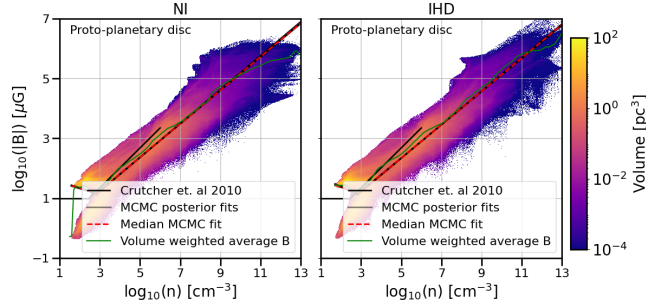


Figure 6. Core collapse to disc simulations: the volume-weighted absolute magnetic field $|\mathbf{B}|$ and number density n distribution from (left) the non-ideal and (right) the ideal MHD simulation of [Lebreuilly et al. \(2021\)](#). The red line is the relation computed using the median parameter values from the 10 MCMC fits. The grey lines show the best-fitting relations from the 10 independent random samples from the data set each consisting of 50,000 points as described in the text (these show little scatter and lie underneath the red line) The black line represents the [Crutcher et al. \(2010\)](#) relation. The green line shows the volume-weighted average B-field strength binned by density. We can see that the best-fitting relation computed from MCMC is similar to the volume-weighted mean B-field curve, and they are both close to $\alpha_2 \simeq 0.5$.

$\alpha_2 = 0.13$. The break occurs between $n_0 \sim 1 \text{ cm}^{-3}$ and $n_0 \sim 60 \text{ cm}^{-3}$, 1 to 2 orders of magnitude below the expected break.

Figure 9 shows results from the PENCIL simulations of [Gent et al. \(2024\)](#) taken at various times to see the effects of the SSD and the large-scale dynamo (LSD), both of which are described in the review by [Korpi-Lagg et al. \(2024\)](#). These simulations include SN feedback, heating and cooling, and, in the case of the LSD simulation, vertical stratification and galactic shear. The SSD simulation has a resolution of 1 pc, while the LSD simulation has a resolution of 4 pc. We plot the magnetic field-density relationship at three times for the SSD simulation: just as the field begins to grow at 35 Myr; when the SSD begins to saturate at 98 Myr; and after the SSD has fully saturated, but before the LSD has had time to grow. We plot the LSD simulation at 3500 Myr, when the LSD is approaching saturation.

Over time, starting in the diffuse medium, a positive α_1 begins to appear. By 98 Myr, SSD_98, $\alpha_1 \sim 0.5$ with α_2 still slightly negative, likely a result of the initial conditions. At ~ 700 Myr, SSD_700, α_1 has become a little smaller, ~ 0.4 , but reaches higher densities where we see the break at $n_0 \sim 0.2 \text{ cm}^{-3}$. The LSD saturates and we see in LSD_3500 $\alpha_1 = 0.5$ and $\alpha_2 = 0.17$, with a break in a similar position in the density to SSD_700. The value of B_0 has increased by a factor of ~ 9 , close to the original value of $10 \mu\text{G}$.

4.3 Isolated galactic simulations

4.3.1 Dwarf galaxies

Figure 10 is taken from the MHD_10 and MHD_SAT low-metallicity dwarf galaxy simulations of [Whitworth et al. \(2023\)](#), which used AREPO. MHD_10 starts with an initially very weak poloidal magnetic seed field of $10^{-6} \mu\text{G}$ and MHD_SAT has an initial poloidal field of $10^{-2} \mu\text{G}$. All simu-

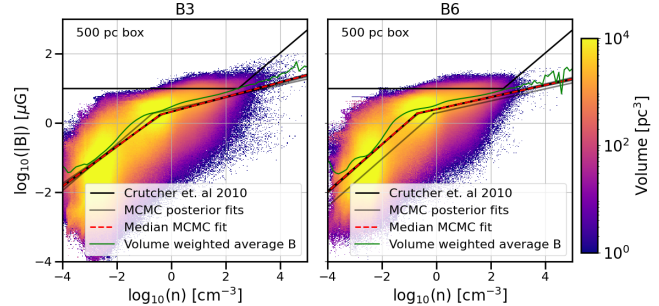


Figure 7. Stratified $(0.5 \text{ kpc})^3$ cube simulations without shear from [Girichidis et al. \(2018\)](#) with initial field strength of (left) $3 \mu\text{G}$ and (right) $6 \mu\text{G}$. The same notation is used as in Figure 6. All of the data in these simulations lie below the Crutcher relationship with a low power-law exponent in the denser gas, a transition at $n \sim 0.3 \text{ cm}^{-3}$, and a larger power-law exponent at low densities.

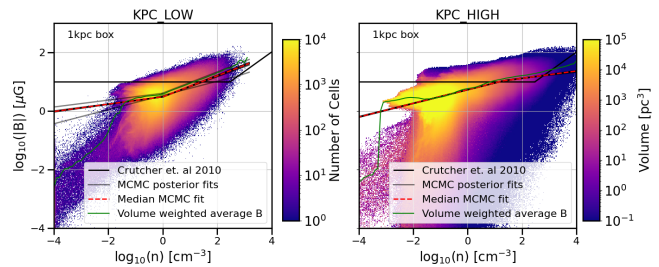


Figure 8. Stratified $(1 \text{ kpc})^3$ cube simulations at 1 kpc scale without shear. The same notation is used as in Figure 6. (Left) the uniform 4 pc resolution simulation of [Brucy et al. \(2023\)](#); (right) the AMR simulation with highest resolution of 0.12 pc of [Colman et al. \(2022\)](#). These simulations do not agree well with the [Crutcher et al. \(2010\)](#) relationship, though the lower resolution simulation does have a larger exponent in the denser gas. There is more scatter in the MCMC results in the diffuse gas. The high resolution simulation appears to be almost a single slope, with only a small decrease in the exponent in the dense region.

lations include self-gravity. The data are taken from the 1 Gyr snapshot.

The plots in Figure 11 come from new, high resolution simulations that use the MHD_10 and MHD_SAT 1 Gyr data from [Whitworth et al. \(2023\)](#) as initial conditions. We describe the new simulations in detail in Appendix B.

MHD_10 has both exponents nearly equal, $\alpha_1 = 0.49$ and $\alpha_2 = 0.45$ with the break density occurring at $n_0 \sim 350 \text{ cm}^{-3}$. In MHD_SAT, initiated with a higher seed field of $10^{-2} \mu\text{G}$, 4 orders of magnitude higher, the diffuse gas exponent is lower, $\alpha_1 \sim 0.36$, and the dense gas exponent is larger, $\alpha_2 \sim 0.91$.

MHD_10_HR shows similar, nearly equal exponents to MHD_10, $\alpha_1 = 0.46$ and $\alpha_2 = 0.46$ but with the break density occurring at much higher values; $n_0 \sim 1460 \text{ cm}^{-3}$. Comparison of MHD_SAT_HR to MHD_SAT shows that the higher resolution simulation has smaller exponents in both diffuse and dense gas, $\alpha_1 \sim 0.28$, and $\alpha_2 \sim 0.55$.

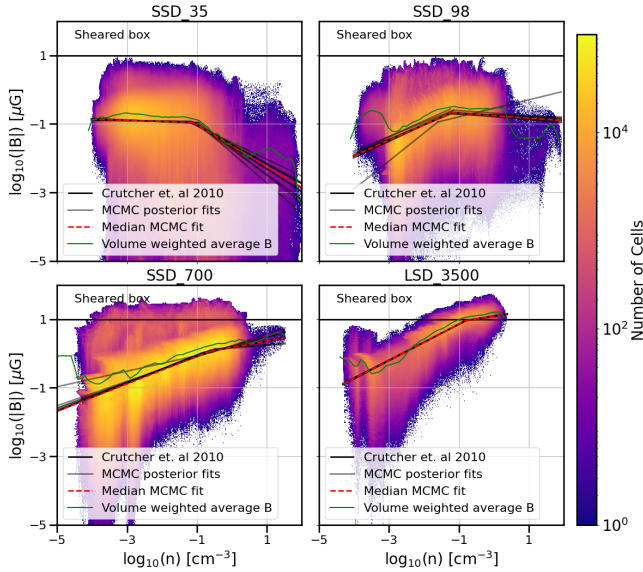


Figure 9. The volume-weighted absolute magnetic field $|\mathbf{B}|$ and number density n distribution of PENCIL simulations of galactic dynamos. The same notation is used as Figure 6. We show three plots where the SSD is dominant at different times from Gent et al. (2024), and one where the LSD has become dominant. We see the effects of the growth of the SSD on the gas from its early kinematic stage at 35 Myr to when it is fully saturated at 700 Myr. We can see at 35 Myr large scatter with a decreasing field strength in dense gas. After 98 Myr we see a rise in the exponent of the slope in the denser gas to near $|\mathbf{B}| = n^0$ and in the diffuse gas it becomes larger. However, after 700 Myr when the SSD and field have had time to grow and reach saturation, we see a power law across most of the gas of $\alpha_1 \sim 0.40$, the break occurs in this simulation towards the denser gas near where there are less cells. After 3500 Myr, the LSD is dominant and we see in this case a power law of $\alpha_1 \sim 0.5$, with a turn over and flattening in the most dense gas.

4.3.2 Milky Way-type galaxies

In Figure 12 we show the results for a Milky Way-like galactic MHD simulation from Robinson & Wadsley (2023) that was simulated using RAMSES. The data is taken after 600 Myr and has a resolution on an AMR grid ranging from 36.6 pc to 9.15 pc in the densest gas. The initial magnetic field was toroidal and set at $1 \mu\text{G}$ (left hand plot) and $0.1 \mu\text{G}$ (right hand plot) at a number density of $n = 0.25 \text{ cm}^{-3}$ with an initial power law index of the field-density relationship $\alpha = 2/3$ across the whole density range and include self-gravity. These simulations evolve the galaxy from this initial state over a period of 250–300 Myr, by which time the disk has settled into a steady state with a star formation rate of a few solar masses per year, as observed. The field saturates to $10\text{--}20 \mu\text{G}$ by the end of the simulation.

The exponents in both simulations have low values for n_0 : 3.17 and 0.06 cm^{-3} respectively. Both have large values for the exponent in the diffuse gas; MW_RAM_1 has $\alpha_1 \sim 0.59$ and MW_RAM_2, has $\alpha_1 \sim 0.81$. The dense gas exponents are similar to the dynamical prediction, MW_RAM_1 has $\alpha_1 \sim 0.43$ and MW_RAM_2, has $\alpha_1 \sim 0.51$.

Figure 13 shows two 3 kpc zoom-in regions of multiscale galactic MHD simulations, using RAMSES and including SN feedback, of Zhao et al. (2024). These are high resolution

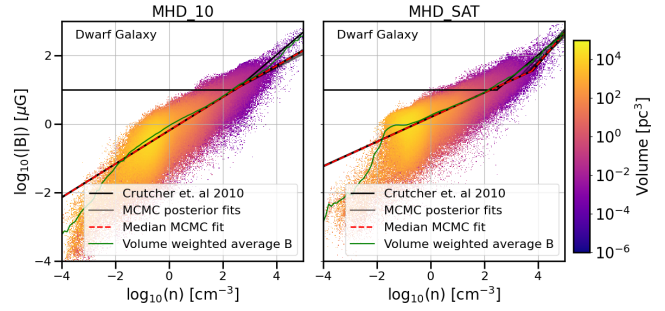


Figure 10. The volume-weighted absolute magnetic field $|\mathbf{B}|$ and number density n distribution for dwarf galaxy simulations MHD_10 and MHD_SAT taken from Whitworth et al. (2023). The same notation is used as Figure 6. Simulation MHD_10 shows an almost singular power-law with $\alpha_1 \sim 0.49$ and a break at the expected $n_0 \sim 350 \text{ cm}^{-3}$. Whereas MHD_SAT is lower in the diffuse gas and much higher in the dense gas with the break occurring much higher.

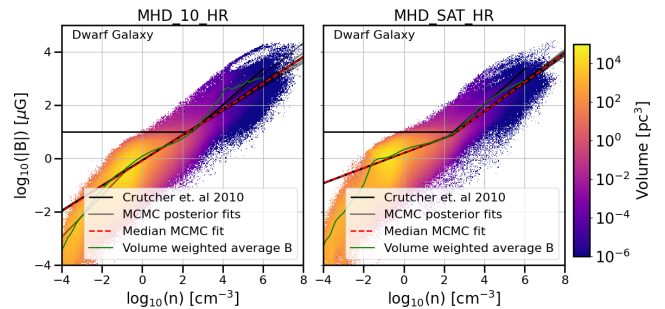


Figure 11. The volume-weighted absolute magnetic field $|\mathbf{B}|$ and number density n distribution for the new high-resolution MHD dwarf galaxy simulations MHD_10_HR and MHD_SAT_HR. The same notation is used as Figure 6. MHD_10_HR again shows a near single power-law exponent with $\alpha \sim 0.5$ with the "break" at $n_0 \sim 1500 \text{ cm}^{-3}$. MHD_SAT_HR shows a clean break at $n_0 \sim 250 \text{ cm}^{-3}$ with a small exponent in the diffuse gas, but not flat, and an exponent of $\alpha_2 \sim 0.5$ in the dense gas.

(grid resolution of 0.286 pc with a mass refinement of $93 M_\odot$), zoom-in boxes of a Milky Way-like simulation whose setup is similar to Robinson & Wadsley (2023) and therefore includes galactic shear and self-gravity. The simulations employ delayed cooling that allows superbubbles to expand for 5 Myrs before being affected by cooling. The zooms focus on two different 3 kpc regions within the galaxy, the *active* simulation is a region of intersecting SN bubbles at a time of 283 Myr (MWR_R2). The *quiet* simulation (MWR_R1) is a (relatively) bubble-less area and follows a portion of a spiral arm at 337 Myr. The dense gas is resolved to $n = 10^6 \text{ cm}^{-3}$.

The most notable difference between the two simulations from Zhao et al. (2024) is in the diffuse gas exponents: MWR_R1 has $\alpha_1 \sim 0.79$ and MWR_R2 shows $\alpha_1 \sim 0.72$. The more turbulent region has a higher value. Both regions have a similar $\alpha_2 \sim 0.5$ and both n_0 and B_0 are similar as well.

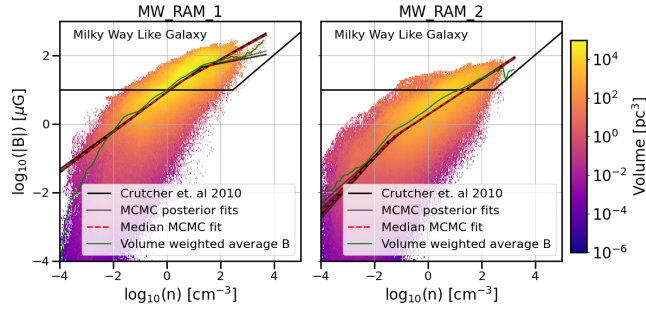


Figure 12. The volume-weighted absolute magnetic field $|B|$ and number density n distribution taken from a Milky Way simulation using RAMSES from [Robinson & Wadsley \(2023\)](#). The same notation is used as Figure 6. The left plot shows a simulation with a higher initial field strength of $1\mu\text{G}$. The right plot starts with a lower field strength of $0.1\mu\text{G}$. Both simulations here show across most of the density range an $\alpha \sim 0.5$ with variation in the top end, α_2 , for the higher initial field simulation, MW_RAM_1, and a greater exponent in the more diffuse gas, α_1 for the higher initial field simulation, MW_RAM_1.

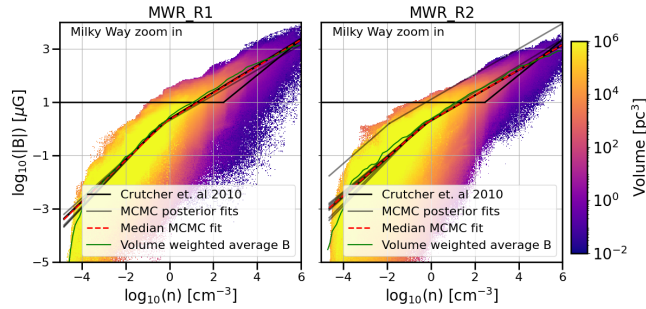


Figure 13. The volume-weighted absolute magnetic field $|B|$ and number density n distribution taken from two, 3 kpc zoom-in regions of Milky Way simulations from [Zhao et al. \(2024\)](#) using RAMSES: Left - an active region dominated by superbubbles, Right - a more quiescent region dominated by a spiral arm segment. The same notation is used as Figure 6. We see that the best-fitting relation computed from MCMC has a large α_1 between ~ 0.7 and 0.8 with a break at $n_0 \sim 0.6$.

5 DISCUSSION

We have presented the magnetic field-density relation derived from observational data and a range of numerical simulations in the previous sections. We now discuss the impact and importance of these results.

5.1 Observations

The original B - n relation has been a useful tool in furthering our understanding of the physics of magnetic fields in the ISM, with its implications for star formation and other processes. However, since it was developed by [Crutcher et al. \(2010\)](#) there has been little further evolution of the approach beyond the use of Zeeman measurements (see [Tritsis et al. 2015; Jiang et al. 2020](#)). No other studies to date have included the DCF data.

With our extended analysis of not only the Zeeman data,

but also 24 years of DCF observational data, we have found that a new form for the relation emerges, which has important consequences. We begin our discussion by considering our treatment of the original Zeeman data and how it differs from the earlier work.

First, a technical point: for all data sets treated here there is little difference between the original reported field strengths in Table 1 and the 3D scaled data in Table 2. This is due to the 3D scale factor for both the DCF and Zeeman data being a factor of ~ 2 . Therefore our discussion shall focus on the 3D data sets.

Beginning with the 3D-Zeeman data set, the power-law exponents α_1 and α_2 are inconsistent with the values proposed in [Crutcher et al. \(2010\)](#), though the high-density exponent α_2 is close with the original 0.66 lying within the 68% credible interval. The low-density exponent α_1 is largely unconstrained due to the large errors on the result, even with the large errors the original flat relationship does not match, hinting that there may be a relationship in diffuse gas. We also find that our value for $n_0 \sim 622 \text{ cm}^{-3}$ is higher and not within the 68% interval of the original result, being over a factor of 2 greater.

One idea as to why the break occurs at the density originally reported, $n_0 \sim 300 \text{ cm}^{-3}$, is that self-gravity becomes important in the kinematics of the ISM at that density. However, this is not a strict value and the break can occur across a range of values depending on many factors within and without the object being studied, such as colliding flows, SN driven shock fronts, and other forms of turbulence. We discuss the break in detail in Section 5.2.

Comparing the individual DCF data sets we find various differences. Data sets 6) 3D-DCF_{sym} and 7) 3D-DCF_{asym} are very similar with each parameter lying within the 65% interval. When we include the KDE estimated errors in data set 8) 3D-DCF_{kde}, there is a significant change in the dense gas exponent, which becomes smaller. Turning to the Scaled data set (9), where we have taken the scaling factor of $c = 6.3$ from [Pattle et al. \(2022\)](#) and applied it to the 3D-DCF data to bring it in line with the 3D-Zeeman data, the results are similar to those of 6) 3D-DCF_{sym} and 7) 3D-DCF_{asym}, see Figure 4, with only B_0 showing significant variation. This is understandable as we have lowered the values on the magnetic field strengths.

Finally, in the Fiducial data set (10), the 3D-DCF data is scaled to be in line with the 3D-Zeeman measurements and combined. The value of α_1 remains the same as that for the 3D-Zeeman data set (5). The dense gas exponent $\alpha_2 = 0.54$, closer to the dynamical exponent. This exponent would be lower if we included data with KDE errors (3D-DCF_{kde}) but due to the uncertainty inherent in the data we do not compare them.

The most interesting finding is the consistency of $\alpha_1 \sim 0.27$ between all the data sets. A more detailed study of the diffuse exponent including detailed error treatment would provide valuable insights. Its value likely provides probes the dynamical nature of magnetic field generation in diffuse gas. We shall discuss this in more detail in the context of numerical simulations in Section 5.4.

5.2 The observed break density

One of the most notable differences between our work and previous studies is the inference of a new free parameter in the statistical analysis. The effect of adding α_1 changes key aspects of the original relationship, most importantly, the value of the break density n_0 .

Both the 1D and 3D Zeeman data sets show a higher value for n_0 compared to the Crutcher result, but similar values for B_0 (see Fig. 4 for a visual comparison). The value of n_0 is higher than the original relationship at $n \sim 620 - 640 \text{ cm}^{-3}$ and does not lie within the 68% credible interval range of the original result. It is similar to Model A proposed by Jiang et al. (2020) in their extended model.

Examining the break in data sets 6) 3D-DCF_{sym} and 7) 3D-DCF_{asym}, the break occurs again at a yet higher value, $n_0 \sim 910 - 920 \text{ cm}^{-3}$. Here we find similar values to Model B in Jiang et al. (2020), which they conclude is their most reliable result. Tritsis et al. (2015) do not report on the break in their models, but only consider data above $n_0 = 300 \text{ cm}^{-3}$.

The most reliable values from our Fiducial data set show the break at $n_0 = 924^{+145}_{-144} \text{ cm}^{-3}$. This break density is significant as it is higher than the value at which molecular gas begins to form.

5.3 The B-n relation from DCF-Zeeman observations

Analysis of our Fiducial data set including both DCF and Zeeman measurements produces a new relation that includes an exponent in the diffuse gas with a break point in number density at $n_0 = 924^{+145}_{-144} \text{ cm}^{-3}$ and magnetic field strength at $B_0 = 9.7 \pm 0.8 \mu\text{G}$:

$$|\mathbf{B}| = B_0 \begin{cases} \left(\frac{n}{n_0}\right)^{0.27 \pm 0.017} & \text{if } n \leq n_0, \\ \left(\frac{n}{n_0}\right)^{0.54 \pm 0.018} & \text{if } n > n_0. \end{cases} \quad (5)$$

5.4 The B-n relation from numerical simulations

When we compare the magnetic field strength to number density across different MHD codes and simulations, we see that they do not show the typical Crutcher et al. (2010) relation of a flat low density relation with a change to $n^{2/3}$ at $n = 300 \text{ cm}^{-3}$. In this section we describe the relations drawn from the simulations and reasons for the deviations seen in each model.

5.4.1 Core collapse simulations

These simulations are sufficiently high resolution to capture the formation of protoplanetary discs, which are much denser than typical regions in molecular clouds, as we see in Figure 6 where $n = 10^{13} \text{ cm}^{-3}$ is reached. The negative α_1 is due to numerical scatter in the most diffuse gas. These simulations do not trace gas below $\sim 500 \text{ cm}^{-3}$, which prevents us from drawing conclusions on the break in the relation and the low density gas exponent α_1 .

The discs are born in an environment undergoing compression through gravitational collapse. This leads to the field dynamically constraining the collapse along field lines, which

gives rise to $\alpha_2 \sim 0.56$. We see no difference in the value between simulations with and without ambipolar diffusion, although we note the presence of a plateau at high density (in a negligible fraction of the volume) for the case with ambipolar diffusion.

5.4.2 Turbulent Box simulations

The two $(0.5\text{kpc})^3$ turbulent box simulations of Girichidis et al. (2018) (Fig. 7) only differ in initial seed field strength. They reach high enough densities that a break at $n_0 = 300 \text{ cm}^{-3}$ could appear, but it actually appears at a lower value of, $n_0 \sim 0.4 \text{ cm}^{-3}$. The diffuse exponent is high whilst the dense exponent is much lower than expected.

There are two reasons that could lead to this result. The first is that the diffuse gas is more turbulent than the dense gas as the simulation is being driven by strong SN feedback. Gent et al. (2021) report that the SSD grows rapidly in hot, diffuse gas, so the high temperatures provided by SNe accelerate field growth. This suggests that not enough SN heating has occurred to allow for the growth of the SSD. The second explanation is that these simulations have run for only 60 Myr, meaning the dynamo has likely not reached saturation and the field is likely still growing. The SSD can take a few tens to hundreds of megayears to saturate depending on numerical resolution (Gent et al. 2021; Whitworth et al. 2023; Gent et al. 2024).

The lack of saturation has an important impact on the dynamics of the ISM, since the lower field reduces the magnetic pressure support, allowing the gas to collapse quicker. Starting with a higher field (see simulation B6, Fig. 7) does not seem to counteract this. As the gas is not hot or turbulent in the initial conditions, the field does not dynamically support the gas. Figure 3 of Robinson & Wadsley (2023) shows their high initial field strength simulation decreasing in field strength over time.

The simulations in Figure 8 have been run for over twice the time as those in Figure 7. Both show a similar small exponent in the dense gas and KPC_LOW shows a small exponent across all densities meaning that evolutionary time could have an effect. The gas is hot and turbulent enough for the SSD to have grown. However, when the resolution is increased in KPC_HIGH and the simulation is run for longer we see a larger exponent in the diffuse gas.

There are a few reasons why this could be happening. One is the change in resolution, as discussed in Section 5.4.4. Since the saturation time for the SSD depends sensitively on numerical resolution down to sub-parsec scales (Gent et al. 2021), a sudden change in resolution will lead to a change in the rate of field amplification. As KPC_HIGH was only run for an additional ~ 20 Myr at higher resolution, this may not be long enough for the B-field to saturate in the new cells.

Another key factor in determining the exponents are the initial conditions. Sur et al. (2012) showed that varying the turbulent driving can lead to a departure from the kinematic exponent, $\alpha_2 = 2/3$. It becomes smaller as the SSD saturates first on small scales, and later at larger scales. Gent et al. (2021) shows that the SSD grows rapidly in a hot turbulent medium. Most simulations start with the gas uniform in temperature and density. Therefore, if simulations are initiated with specific seed field configurations, then the diffuse

end will likely drop due to a lack of a hot, diffuse, turbulent medium.

Important processes are missing from these simulations. In particular, galactic rotation and shear are key in the growth of the LSD in galaxies, which offers support to the field over much longer time-scales. On shorter time scales shear may affect the gas distribution through large-scale rotational effects.

5.4.3 Galactic rotation

The dwarf galaxy simulations of [Whitworth et al. \(2023\)](#), shown in Figure 10, have a range in density from $n = 10^{-4} \text{ cm}^{-3}$ to 10^5 cm^{-3} comparable to that covered by the Zeeman observations. We see that MHD_SAT has a smaller diffuse gas exponent, α_1 , and a larger dense gas exponent, α_2 , than MHD_10. This suggests that the relationship is connected to the initial conditions. We confirm this by noting that MHD_SAT has a larger initial seed field, $10^{-2} \mu\text{G}$, which, as seen in Figure 5 of [Whitworth et al. \(2023\)](#), results in a field with large-scale order and higher strength in the diffuse regions.

If a simulation is initiated with a stronger field then the gas is supported dynamically for longer. This leads to the diffuse gas starting with a higher field, giving rise to a lower value for α_1 . This is in opposition to the turbulent box simulations and is likely an effect of scales, both physical and temporal. Galaxy simulations usually produce data every megayear with resolutions of a few parsecs, whereas turbulent boxes have finer time and spatial resolution, allowing them to better model small perturbations in field amplification.

Figure 12 shows the results from a Milky Way scale simulation. As in the case of the dwarf galaxy simulations, the diffuse gas field strength has dropped below the initial field strength. This suggests the SSD is not active enough to amplify the field here. This may be a resolution problem, as the diffuse gas is under-resolved, meaning the SSD cannot be accurately modelled (see [Martin-Alvarez et al. 2022](#), for discussion of this issue). We discuss this in Section 5.4.4 below.

Figure 2 in [Robinson & Wadsley \(2023\)](#) compares the time evolution of the B - n relationship for different initial field strengths. In the case of a weak or medium initial seed field, α_2 tends to 0.5. In the strong field case the diffuse gas remains at $\alpha_1 = 2/3$ but α_2 is smaller. The important point here is that simulations with weak initial fields grow naturally by dynamo action resulting in the best fits to the observations. Imposing artificially strong initial fields has adverse effects on star formation and the final saturated state of the field.

Large-scale dynamo action in Milky Way galaxies depends on rotational time scales, which are much longer than the eddy time on which the SSD grows. It is expected to take of the order of 5–10 rotations ([Pfrommer et al. 2022; Gent et al. 2024](#)) for the LSD to become the dominant source of magnetic field support. The rotational period of the dwarf galaxies is on the order of 400 Myr ([Whitworth et al. 2023](#)), with a similar dynamical time in the simulations of [Robinson & Wadsley \(2023\)](#). As these simulations only run for 1 Gyr, this likely means that LSD effects are not yet dominant.

The simulations in Figure 9 track the effects of dynamo evolution over 3500 Myr. We see that as the dynamo evolves from the SSD in the early stages (~ 35 Myr) to the LSD at late times (~ 3500 Myr), the main exponent tends to $\alpha_1 \simeq 0.5$.

Though we can not say much about the dense gas exponent from these simulations, we can be confident in saying a non-zero exponent in the diffuse gas is possible and can arise purely from dynamo activity. It is interesting to note that these simulations do not include self-gravity, implying that the B - n relation found here is purely driven by dynamo activity driven by feedback and shear.

In summary, we have shown that all simulations that include large scale galactic rotation tend towards an exponent of ~ 0.5 . This can appear in either the diffuse gas exponent α_1 or the dense gas exponent α_2 in the results depending on the set up of the simulation and density range being captured.

5.4.4 Resolution effects on the dynamo

[Ibáñez-Mejía et al. \(2022\)](#) showed in high resolution zoom-in MHD simulations of clouds in a rotating galaxy that molecular clouds are magnetically supported with a field parallel to the density gradient. In all three clouds they simulate, each has an exponent of less than $\alpha = 0.5$ with no break in the B - n relationship. The diffuse gas is well resolved in these simulations, so how important is resolution in the diffuse gas?

Most numerical simulations of the ISM on large scales lack resolution in diffuse gas. Of the simulations presented here, two resolve the diffuse gas to scales where the SSD should be captured: the dynamo simulation of [Gent et al. \(2024\)](#) (SSD_35, SS_98 and SSD_700) with a uniform 1 pc^2 cell resolution, and the Milky Way like zoom-in simulation of [Zhao et al. \(2024\)](#) with a uniform 0.29 pc^2 resolution. This is important as the SSD works on scales smaller than 1 pc ([Korpi-Lagg et al. 2024](#)).

Resolving the SSD is important in order to track the rapid amplification intrinsic to turbulent dynamo theories. A stronger field will support the diffuse gas against collapse similar to the way a strong field in dense gas slows its collapse and suppresses star formation ([Hennebelle & Inutsuka 2019](#)).

In the time evolving SSD PENCIL simulation (Fig. 9), α_1 tends towards a value of 0.5. This is a stratified box simulation with shear effects, not a full galactic disc, but it does have a dense mid-plane with diffuse gas bubbles (see Figures 1, 3 and 13 in [Gent et al. 2024](#)). This shows that given enough time, on the order of a few hundred megayears in a simulation with a rotation rate twice that of the Milky Way (so around 5 rotation periods), along with shear, an exponent of $\alpha_1 \simeq 0.5$ can develop.

The high resolution dwarf galaxy simulations MHD_10_HR and MHD_SAT_HR, Figure 11, show little difference in the low density exponents compared to the original simulations of [Whitworth et al. \(2023\)](#), Figure 10. This is due to the diffuse gas still not being well resolved, only reaching parsec scale resolution at $n > 10 \text{ cm}^{-3}$. See Appendix C for a detailed look at the resolved diffuse gas in the dwarf galaxy simulations.

The zoom in regions of [Zhao et al. \(2024\)](#) (Fig. 13) have a similar exponent in both the dense and diffuse gas. However, the turbulent region, MWR_R2, has a larger exponent, adding support to the idea that turbulence is driving the relationship.

In summary, for all the simulations presented here that have had enough time for the SSD or LSD to reach saturation, the exponent tends to $\alpha \propto 0.5$. This can be in either α_1 or α_2 depending on the simulation set up and density range

covered. We see little evidence of the expected $\alpha \sim 0.66$ for kinematic collapse. All of these simulations are disc-like, rotating, use the ideal-MHD approximation, and are not uniformly gravitationally collapsing. This suggests that the exponent of ~ 0.50 can be a consequence of a saturated large-scale dynamo as well as of a dynamical collapse. The simulations that are non-rotating, younger and/or less resolved show a more varied array of exponents dependant on the initial seed field implementation and simulation time.

5.5 The numerical break density

Only a few of the simulations presented here allow us to confidently draw any conclusions about the break density n_0 , due to the density ranges they cover. Simulations that do not span a density range above or below $n \simeq 100 \text{ cm}^{-3}$ (where gas becomes dense) by a few orders of magnitude will likely give misleading results. For example, in the protoplanetary disc population simulations NI and IMHD, we find $n_0 \sim 707 \text{ cm}^{-3}$ which is close to the lowest density. Conversely, the PENCIL simulations don't achieve densities of $n_0 \sim 300 \text{ cm}^{-3}$ meaning no break is likely to be found at the expected density.

Over all, we find much variability in the position of the break density in simulations that span the density range of the observational data sets. These are the simulations KPC_HIGH, MHD_10_HR, MHD_SAT_HR, MWR_R1, MWR_R2 and possibly MHD_10 and MHD_SAT. The lowest n_0 found in these simulations is $n_0 \simeq 0.64 \text{ cm}^{-3}$, MWR_R1, whilst the highest is $n_0 \simeq 5666.70 \text{ cm}^{-3}$, MHD_SAT. This is a difference of four orders of magnitude. The dwarf galaxy simulations MHD_SAT and MHD_10_HR predict a break within the 68% interval of the Fiducial observational result for n_0 , whilst MHD_10 and MHD_SAT_HR show a result similar to the original result. The values for B_0 are less well matched in all simulations. Values range from $B_0 \sim 0.11 \mu\text{G}$ in SSD_35 to $B_0 \sim 35 \mu\text{G}$ in MHD_SAT.

The break density appears to be dependent on several key factors, including resolution, initial seed field strength and time. To better constrain the break point in numerical simulations we need better estimates on the errors, not just for B , but for n as well. We leave this for future studies.

5.6 Numerical caveats

A consideration for any numerical simulation is the effect of numerical diffusion due to finite resolution. In magnetic field studies this is particularly important due to the effects at small scales where resistivity becomes important. None of the simulations presented here are resolved well enough to completely overcome this. We can however consider what happens when resolution is improved (Fig. 14). MHD_10_LR is taken from the Appendix of Whitworth et al. (2023) and has a much lower resolution than MHD_10 with a Jeans refinement of 4 cells instead of 8, a cell mass of 500 M_\odot , and a sink creation density threshold of 10^2 cm^{-3} . Whilst the dense gas exponent is $\alpha_2 \sim 0.50$, the diffuse exponent becomes much larger, $\alpha_1 \sim 0.83$. As we increase the resolution up to the high resolution simulation MHD_10_HR, α_1 tends to 0.50 and n_0 increases closer to that found by observation.

Another caveat is that the simulation results do not have

errors. We have implemented errors based on the KDE method as described in Appendix A3. Comparing the results of the MCMC to the volume weighted average magnetic field binned via density, the plotted green lines, we see that they match quite closely. By including the nuisance factor $\ln V$ in the MCMC we mitigate some of the issues that will arise due to poor error treatment.

6 SUMMARY AND CONCLUSIONS

By using observational data sets that include both Zeeman and DCF measurements and expanding the number of free parameters in the fit, we have shown a divergence from the B - n relation found by Crutcher et al. (2010). This is most clearly seen in the power-law exponent for the diffuse gas, where we find $\alpha_1 \sim 0.27 \pm 0.017$ for our Fiducial model, rather than $\alpha_1 = 0$. We find a dense gas exponent of $\alpha_2 \sim 0.54 \pm 0.018$, lower than the value $\alpha \simeq 0.66$ found by Crutcher et al. (2010) but slightly larger than the dynamical collapse exponent $\alpha_2 \simeq 0.5$. We also find a higher value than Crutcher et al. (2010) for the break density $n_0 = 924^{+145}_{-144}$.

The numerical simulations have a wide range of parameters for the B - n relation. They appear to depend on the system being studied. To reproduce the observed results, a saturated galactic dynamo must be resolved in both the diffuse and dense gas, requiring a spatial resolution below 1–2 pc and a time scale of a few hundred megayears. Thus, it appears that the relation is not strongly tied to the self-gravity of the system. Rather, it is driven by the dynamo, feedback, and turbulence in line with previous work (Gazol & Villagran 2018). We see this from the sheared turbulent box simulations of Gent et al. (2024), which do not include self-gravity. The inclusion of gravity changes the value of the break density, but not the overall exponent. This is inline with theoretical ideas (Passot & Vázquez-Semadeni 2003) that show the B - n relation should occur in a wide range of densities.

We summarise our key findings:

- We find a two-part power-law relation differing from that found by Crutcher et al. (2010) for the observational data that includes the new DCF data:

$$|\mathbf{B}| = B_0 \begin{cases} \left(\frac{n}{n_0}\right)^{\alpha_1} & \text{if } n \leq n_0, \\ \left(\frac{n}{n_0}\right)^{\alpha_2} & \text{if } n > n_0. \end{cases} \quad (6)$$

where $B_0 = 9.7 \pm 0.8 \mu\text{G}$, $n_0 = 924^{+145}_{-144} \text{ cm}^{-3}$, $\alpha_1 = 0.27 \pm 0.017$, and $\alpha_2 = 0.54 \pm 0.018$.

- The observed exponent in the dense gas, α_2 , is closer to the dynamic exponent of 1/2 than the kinematic exponent of 2/3.
- The observed break density occurs at higher densities than found by Crutcher et al. (2010), with large error bars reflecting the highly variable dynamical and anisotropic state of the ISM.
- The simulations that match the observed B - n relation best – the dwarf galaxy and Milky Way like simulations – have a consistent exponent of $\alpha_2 \simeq 0.5$ in the dense gas, with variability in the diffuse gas exponent α_1 .
- Resolving the diffuse medium in MHD simulations provides more accurate modelling of the magnetic field, magnetic support and effects of the small and large-scale dynamo.

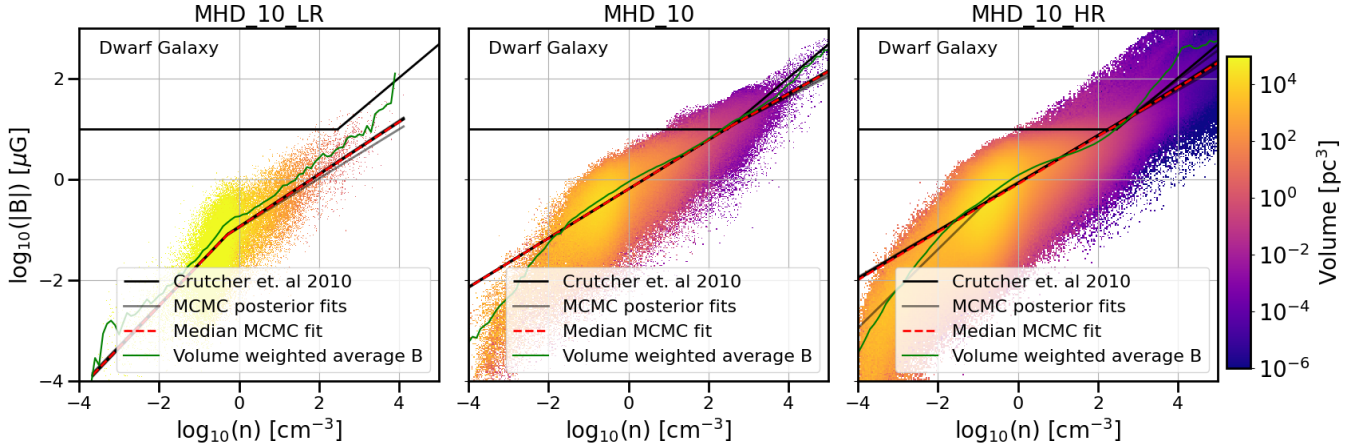


Figure 14. The $|B|$ - n distribution for three dwarf galaxy simulations with varying numerical resolution: the low resolution dwarf galaxy simulation from the Appendix of Whitworth et al. (2023), MHD_Low, MHD_10, and the new high-resolution MHD_10_HR. The same notation is used as Figure 6. This comparison shows the effects of numerical diffusion. As the simulation becomes more resolved, the relationship for both exponents tends to $\alpha_1 \simeq \alpha_2 \simeq 0.5$.

- The B - n relation found in the simulations is a time-averaged result driven by multiple turbulent effects including shear and SN driving in hot, diffuse gas.
- Simulations with saturated large-scale dynamo show an exponent of 0.5 even in the absence of self-gravity and thus dynamical collapse.
- To better understand the behaviour of magnetic fields on gas within galaxies we need more data from both observations and numerical simulations, the latter addressing some of the limitations that we have noted.

ACKNOWLEDGEMENTS

We thank the members of the AREPO ISM group and ECO-GAL Large Scale Structures group for discussions and insightful comments on the coding and science goals in this paper. We also thank V. Springel for access to AREPO and R. Treß for the development of the photoionization code used in this work. DJW acknowledges support from the Programa de Becas Posdoctorales of the Dirección General de Asuntos del Personal Académico of the Universidad Nacional Autónoma de México (DGAPA,UNAM,Mexico). SS acknowledges support from UNAM-PAPIIT Program IA10484. REP is supported by a Discovery Grant from NSERC, Canada. He is also grateful for support of his sabbatical leave in Heidelberg (2022/23), by the Institute for Theoretical Astrophysics of the University of Heidelberg (ITA) and the Max Planck Institute for Astronomy, where this work was started. RJS gratefully acknowledges an STFC Ernest Rutherford fellowship (grant ST/N00485X/1). M-MML acknowledges direct support from US National Science Foundation grants AST18-15461 and AST23-07950, as well as support from grant PHY23-09135 to the Kavli Institute for Theoretical Physics. LSV was supported by the Science Pathways Scholars Program of Barnard College. RP acknowledges funding support from Ontario Graduate Scholarships and the Queen Elizabeth II Graduate Scholarship in Science & Technology. AP acknowledges financial support from the grant UNAM-

PAPIIT IG100223, the Sistema Nacional de Investigadores of CONAHCyT, and from the CONAHCyT project number 86372 of the ‘Ciencia de Frontera 2019’ program, entitled ‘Cítlalcoatl: A multiscale study at the new frontier of the formation and early evolution of stars and planetary systems’, México.

DJW, PG, NB, UL, PH, RK, acknowledge funding from the European Research Council via the ERC Synergy Grant “ECOGAL” (project ID 855130), from the Deutsche Forschungsgemeinschaft (DFG) via the Collaborative Research Center “The Milky Way System” (SFB 881 – funding ID 138713538 – subprojects A1, B1, B2 and B8), from the German Excellence Strategy via the Heidelberg Cluster of Excellence “STRUCTURES” (EXC 2181 - 390900948), and from the German Ministry for Economic Affairs and Climate Action in project “MAINN” (funding ID 50OO2206). They also acknowledge computing resources provided by *The Land* and the DFG through grant INST 35/1134-1 FUGG and for data storage at SDS@hd through grant INST 35/1314-1 FUGG.

This work used the DiRAC COSMA Durham facility managed by the Institute for Computational Cosmology on behalf of the STFC DiRAC HPC Facility (www.dirac.ac.uk). The equipment was funded by BEIS capital funding via STFC capital grants ST/P002293/1, ST/R002371/1 and ST/S002502/1, Durham University and STFC operations grant ST/R000832/1. DiRAC is part of the National e-Infrastructure. The research conducted in this paper used SciPy ([Virtanen et al. 2020](https://www.scipy.org)), NumPy ([van der Walt et al. 2011](https://numpy.org)), and matplotlib, a Python library used to create publication quality plots ([Hunter 2007](https://matplotlib.org)).

DATA AVAILABILITY

The dwarf galaxy data is available upon request to the first author. For all other data the reader will need to contact the owner of that data as listed in the appropriate reference.

The code used for the Bayesian analysis can be supplied by the first author upon request.

REFERENCES

Banerjee R., Vázquez-Semadeni E., Hennebelle P., Klessen R. S., 2009, *MNRAS*, **398**, 1082

Beck R., 2015, *A&ARv*, **24**, 4

Brandenburg A., Dobler W., 2002, *Computer Physics Communications*, **147**, 471

Brandenburg A., et al., 2020, *Journal of Open Source Software*, **6**, 7

Brucy N., Hennebelle P., Colman T., Iteanu S., 2023, *A&A*, **675**, A144

Camacho V., Vázquez-Semadeni E., Palau A., Zamora-Avilés M., 2023, *MNRAS*, **523**, 3376

Carilli C. L., Taylor G. B., 2002, *ARA&A*, **40**, 319

Chandrasekhar S., Fermi E., 1953, *ApJ*, **118**, 113

Colman T., et al., 2022, *MNRAS*, **514**, 3670

Commerçon B., González M., Mignon-Risse R., Hennebelle P., Vaytet N., 2022, *A&A*, **658**, A52

Crutcher R. M., 2004, in Uyaniker B., Reich W., Wielebinski R., eds, *The Magnetized Interstellar Medium*. pp 123–132

Crutcher R. M., 2012, *ARA&A*, **50**, 29

Crutcher R. M., Nutter D. J., Ward-Thompson D., Kirk J. M., 2004, *ApJ*, **600**, 279

Crutcher R. M., Wandelt B., Heiles C., Falgarone E., Troland T. H., 2010, *ApJ*, **725**, 466

Davis L., 1951, *Physical Review*, **81**, 890

Foreman-Mackey D., Hogg D. W., Lang D., Goodman J., 2013, *PASP*, **125**, 306

Fryxell B., et al., 2000, *ApJS*, **131**, 273

Gazol A., Villagrán M. A., 2018, *MNRAS*, **478**, 146

Gent F. A., Mac Low M.-M., Käpylä M. J., Singh N. K., 2021, *ApJ*, **910**, L15

Gent F. A., Mac Low M.-M., Korpi-Lagg M. J., 2024, *ApJ*, **961**, 7

Girichidis P., Seifried D., Naab T., Peters T., Walch S., Wünsch R., Glover S. C. O., Klessen R. S., 2018, *MNRAS*, **480**, 3511

Girma E., Teyssier R., 2023, arXiv e-prints, p. arXiv:2311.10826

Heitsch F., Zweibel E. G., Mac Low M.-M., Li P., Norman M. L., 2001, *ApJ*, **561**, 800

Hennebelle P., Inutsuka S.-i., 2019, *Frontiers in Astronomy and Space Sciences*, **6**, 5

Hennebelle P., Banerjee R., Vázquez-Semadeni E., Klessen R. S., Audit E., 2008, *A&A*, **486**, L43

Hennebelle P., Commerçon B., Lee Y.-N., Charnoz S., 2020, *A&A*, **635**, A67

Hildebrand R. H., Kirby L., Dotson J. L., Houde M., Vaillancourt J. E., 2009, *ApJ*, **696**, 567

Houde M., Vaillancourt J. E., Hildebrand R. H., Chitsazzadeh S., Kirby L., 2009, *ApJ*, **706**, 1504

Hull C. L. H., Zhang Q., 2019, *Frontiers in Astronomy and Space Sciences*, **6**, 3

Hunter J. D., 2007, *Computing in Science Engineering*, **9**, 90

Ibáñez-Mejía J. C., Mac Low M.-M., Klessen R. S., 2022, *ApJ*, **925**, 196

Jiang H., Li H.-b., Fan X., 2020, *ApJ*, **890**, 153

Kirk H., Klassen M., Pudritz R., Pillsworth S., 2015, *ApJ*, **802**, 75

Konstantinou A., Ntormousi E., Tassis K., Pallottini A., 2024, arXiv e-prints, p. arXiv:2402.10268

Korpi-Lagg M. J., Mac Low M.-M., Gent F. A., 2024, arXiv e-prints, p. arXiv:2401.04015

Lazarian A., 2020, *ApJ*, **902**, 97

Lebreuilly U., Hennebelle P., Colman T., Commerçon B., Klessen R., Maury A., Molinari S., Testi L., 2021, *ApJ*, **917**, L10

Li J., Jiang B., Zhao H., Chen X., Yang Y., 2024, arXiv e-prints, p. arXiv:2402.10431

Liu J., et al., 2019, *ApJ*, **877**, 43

Liu J., Zhang Q., Commerçon B., Valdivia V., Maury A., Qiu K., 2021, *ApJ*, **919**, 79

Liu J., Zhang Q., Qiu K., 2022, *Frontiers in Astronomy and Space Sciences*, **9**, 943556

Mac Low M.-M., Klessen R. S., 2004, *Rev. Mod. Phys.*, **76**, 125

Martin-Alvarez S., Devriendt J., Slyz A., Sijacki D., Richardson M. L. A., Katz H., 2022, *MNRAS*

Masson J., Chabrier G., Hennebelle P., Vaytet N., Commerçon B., 2016, *A&A*, **587**, A32

Mestel L., 1966, *MNRAS*, **133**, 265

Moscadelli L., Sanna A., Beuther H., Oliva A., Kuiper R., 2022, *Nature Astronomy*, **6**, 1068

Mouschovias T. C., 1976, *ApJ*, **207**, 141

Mouschovias T. C., Ciolek G. E., 1999, in Lada C. J., Kylafis N. D., eds, *NATO Advanced Study Institute (ASI) Series C Vol. 540, The Origin of Stars and Planetary Systems*. p. 305

Ossenkopf V., Henning T., 1994, *A&A*, **291**, 943

Ostriker E. C., Stone J. M., Gammie C. F., 2001, *ApJ*, **546**, 980

Palau A., et al., 2021, *ApJ*, **912**, 159

Passot T., Vázquez-Semadeni E., 2003, *A&A*, **398**, 845

Pattle K., Fissel L., Tahani M., Liu T., Ntormousi E., 2022, arXiv e-prints, p. arXiv:2203.11179

Pfrommer C., Werhahn M., Pakmor R., Girichidis P., Simpson C. M., 2022, *MNRAS*, **515**, 4229

Pillai T., Kauffmann J., Tan J. C., Goldsmith P. F., Carey S. J., Menten K. M., 2015, *The Astrophysical Journal*, **799**, 74

Planck Collaboration et al., 2016, *A&A*, **586**, A138

Pudritz R. E., Klassen M., Kirk H., Seifried D., Banerjee R., 2014, in Petit P., Jardine M., Spruit H. C., eds, *Magnetic Fields throughout Stellar Evolution Vol. 302, Magnetic Fields throughout Stellar Evolution*. pp 10–20, doi:10.1017/S174392131400163X

Robinson H., Wadsley J., 2023, arXiv e-prints, p. arXiv:2310.15244

Seifried D., Walch S., Weis M., Reissl S., Soler J. D., Klessen R. S., Joshi P. R., 2020, *MNRAS*, **497**, 4196

Skalidis R., Tassis K., 2021, *A&A*, **647**, A186

Skalidis R., Sternberg J., Beattie J. R., Pavlidou V., Tassis K., 2021, *A&A*, **656**, A118

Soler J. D., 2019, *A&A*, **629**, A96

Springel V., 2010, *MNRAS*, **401**, 791

Sur S., Federrath C., Schleicher D. R. G., Banerjee R., Klessen R. S., 2012, *MNRAS*, **423**, 3148

Teyssier R., 2002, *A&A*, **385**, 337

Tritsis A., Panopoulou G. V., Mouschovias T. C., Tassis K., Pavlidou V., 2015, *MNRAS*, **451**, 4384

Vaytet N., Commerçon B., Masson J., González M., Chabrier G., 2018, *A&A*, **615**, A5

Virtanen P., et al., 2020, *Nature Methods*, **17**, 261

Whitworth D. J., Smith R. J., Klessen R. S., Mac Low M.-M., Glover S. C. O., Tress R., Pakmor R., Soler J. D., 2023, *MNRAS*, **520**, 89

Whitworth D. J., Smith R. J., Glover S. C. O., Tress R., Klessen R. S., Feng J., Brucy N., 2024, *MNRAS*

Zhao B., Pudritz R. E., Pillsworth R., Robinson H., Wadsley J., 2024, arXiv e-prints, p. arXiv:2405.18474

van der Walt S., Colbert S. C., Varoquaux G., 2011, *Computing in Science Engineering*, **13**, 22

APPENDIX A: BAYESIAN ANALYSIS

We perform the Bayesian inference with MCMC sampling using the `emcee` code (Foreman-Mackey et al. 2013) on both the observational and numerical data in the roughly the same way, with only some variation in the treatment of the errors and in the initial setup of the likelihood based on the model

and the prior distributions for the parameters. In this section we present the method we implemented.

Bayes' theorem can be summarised in the form:

$$\text{posterior} \times \text{evidence} = \text{prior} \times \text{likelihood} \quad (\text{A1})$$

For a given model, the posterior distribution of the parameters $\theta = (\theta_1, \theta_2, \dots)$ can be written as

$$p(\theta|D) = \frac{p(D|\theta)p(\theta)}{p(D)} \quad (\text{A2})$$

With $p(D|\theta)$ the likelihood, $p(\theta)$ the prior distribution of the parameters, and $p(D)$ the evidence for data D .

A1 Parameters, Likelihood and Posteriors

As in Crutcher et al. (2010) and following works we assume a broken power-law as our underlying model, which is implemented in the likelihood in the MCMC. We do not consider the low density regime to be flat but allow its power-law index to vary along with all other parameters. The model y_{mod} for the magnitude of the magnetic field then becomes:

$$|\mathbf{B}| = y_{\text{mod}}(\theta) = B_0 \begin{cases} (n/n_0)^{\alpha_1} & \text{if } n \leq n_0, \\ (n/n_0)^{\alpha_2} & \text{if } n > n_0. \end{cases} \quad (\text{A3})$$

Our parameters are thus

$$\theta = (\alpha_1, \alpha_2, n_0, B_0, \ln V), \quad (\text{A4})$$

where n_0 is the number density at which the power-law changes, α_1 and α_2 are the power-law indexes below and above n_0 , B_0 is the magnitude of the magnetic field at n_0 , and $\ln V$ is the nuisance factor applied to the errors to account for intrinsic variance not described by the measurement uncertainties.

Assuming that the measurement uncertainties are Gaussian, the likelihood function given a data set $\{y_i\}$ of n points is

$$\ln p(\theta|\{y_i\}) = -\frac{1}{2} \sum_{i=1}^n \left[\left(\frac{y_i - y_{\text{mod}}(\theta)}{s_i} \right)^2 + \ln s_i^2 \right] + \text{constant}, \quad (\text{A5})$$

where θ are the free parameters, y_{mod} is the model as defined in Equation A3 and s_i^2 is:

$$s_i^2 = \sigma_i^2 + V^2 y_{\text{mod}}^2, \quad (\text{A6})$$

where σ_i are the measurement errors on the magnetic field.

For the Zeeman data we use Equation A16 describe in Section A3.

The posterior distribution is proportional to the product of the likelihood and the prior:

$$p(\alpha_1, \alpha_2, n_0, B_0, \ln V|y, \sigma) \propto p(y, \sigma|\alpha_1, \alpha_2, n_0, B_0, \ln V) \times p(\alpha_1)p(\alpha_2)p(n_0)p(B_0)p(\ln V) \quad (\text{A7})$$

where the priors are assumed to be independent.

A2 A study of the priors

In Crutcher et al. (2010) a flat PDF was used for the prior distribution. They also defined a confidence value, f , to the prior in their free parameters for the likelihood function. In Jiang et al. (2020) they show that if $f \geq 2$ then it is difficult to predict the relationship. In this work we do not include f , but instead test three different prior distributions to investigate their effects on the posterior distribution.

We first test independent, truncated uniform priors for all parameters θ . We do this as we have little knowledge of how adding in a new free parameter for the diffuse gas will shape the results. Our choice for the range in α_1 goes from -1 to 1 to account for any exponent that could arise. We use the same range for α_2 as we do not know how it will be affected by α_1 . We keep n_0 and B_0 broad but not unphysical and set $\ln V$ to a large range as again we have no prior knowledge on it:

$$\begin{aligned} p(\alpha_1) &= U(-1.0, 1.0) \\ p(\alpha_2) &= U(-1.0, 1.0) \\ p(n_0) &= U(0.0, 10^5) \\ p(B_0) &= U(10^{-5}, 1000) \\ p(\ln V) &= U(-5.0, 5.0), \end{aligned} \quad (\text{A8})$$

We run the MCMC analysis for 200000 steps based on 100 random walkers, remove the first 100000 for a burn-in period and thin to every two hundredth result to avoid auto-correlation. We do this on the Zeeman line-of-sight data and present the results in Table A1. The errors are large on α_1 in the and the value for n_0 is high. We note that for the posterior samples, Figure A1, their distribution is not well constrained given their large scatter and unclear distributions. We therefore discard this prior for the observational data.

We next test a more constrained flat prior. Our motivation is as follows. By stating a range of -1 to 1 for both α_1 and α_2 , we are assuming that the probability of α_1 laying between, e.g., $-1 \sim -0.8$, is the same as it laying between $0.8 \sim 1.0$, which is unlikely. Previous studies that use different data, and knowledge of physically meaningful values of our parameters, we limit each parameter to:

$$\begin{aligned} p(\alpha_1) &= U(-0.25, 0.75) \\ p(\alpha_2) &= U(0.0, 1.0) \\ p(n_0) &= U(0.1, 1000) \\ p(B_0) &= U(0.5, 100) \\ p(\ln V) &= U(-5.0, 5.0), \end{aligned} \quad (\text{A9})$$

where $U(\min, \max)$ is the truncated uniform distribution.

We rerun the MCMC analysis with these new priors again on the Zeeman data and get results as presented in Table A2. Here we run for 25000 steps with the same 100 random walkers and remove the first 5000 for a burn-in period, thinning to every twentieth result. We do this as we find that the code converges much quicker. The results are similar to the unconstrained results. Looking at the corner plot for the Zeeman data, Figure A2, whilst the distribution is more constrained,

Data set	α_1	α_2	n_0	B_0	$\ln V$
1	$0.276^{+0.119}_{-0.161}$	$0.712^{+0.068}_{-0.076}$	$1953.512^{+1882.972}_{-1307.542}$	$1.988^{+3.154}_{-1.400}$	$1.440^{+1.082}_{-0.634}$

Table A1. The median and 68% Bayesian credible interval for each parameter from the MCMC posterior samples. These results are based on the broad unconstrained flat PDF prior. The results are for the line of sight Zeeman data only.

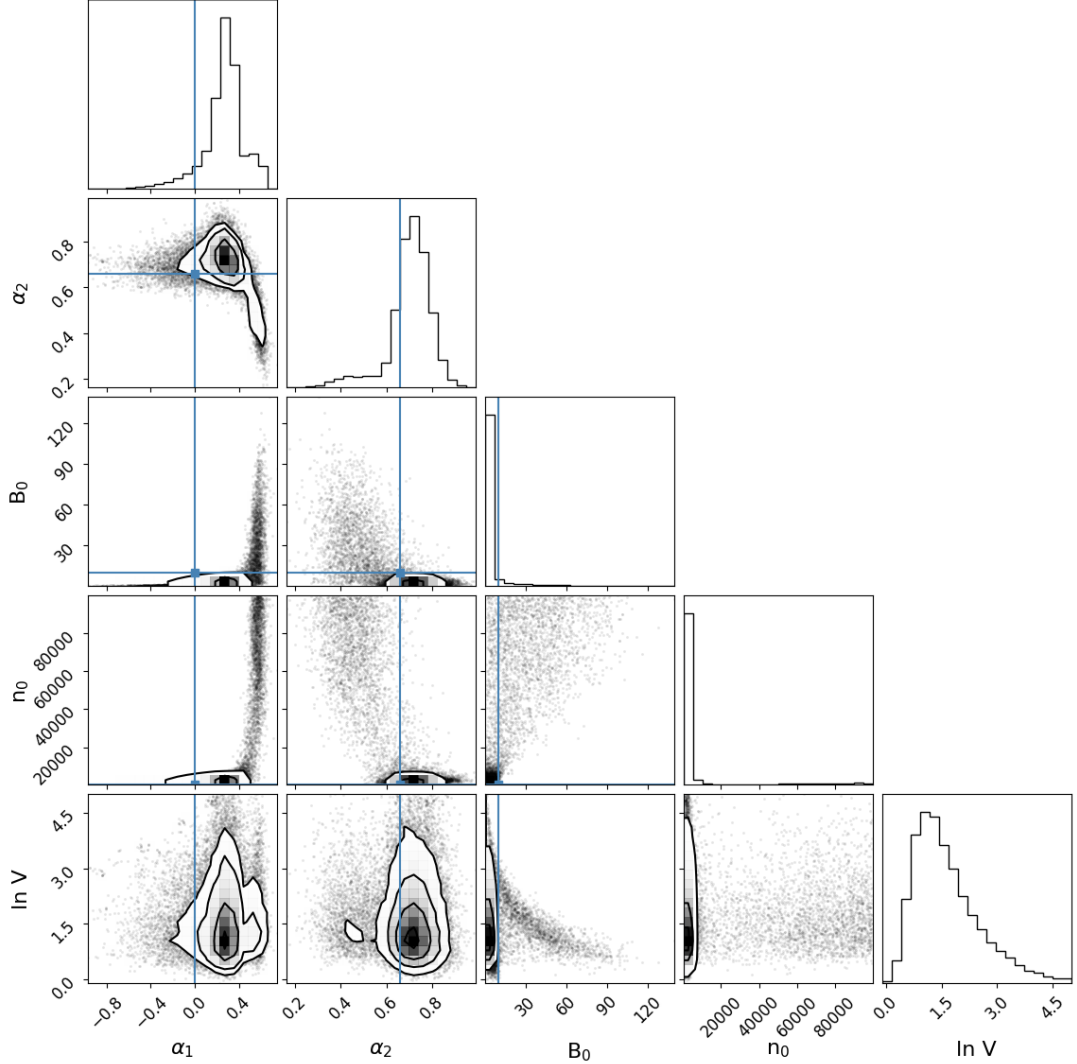


Figure A1. A corner plot for data set 1, Zeeman, using the flat prior in Equation A8. We can see here the posterior distribution is scattered and non-uniform showing that the prior is not well constrained for this data set.

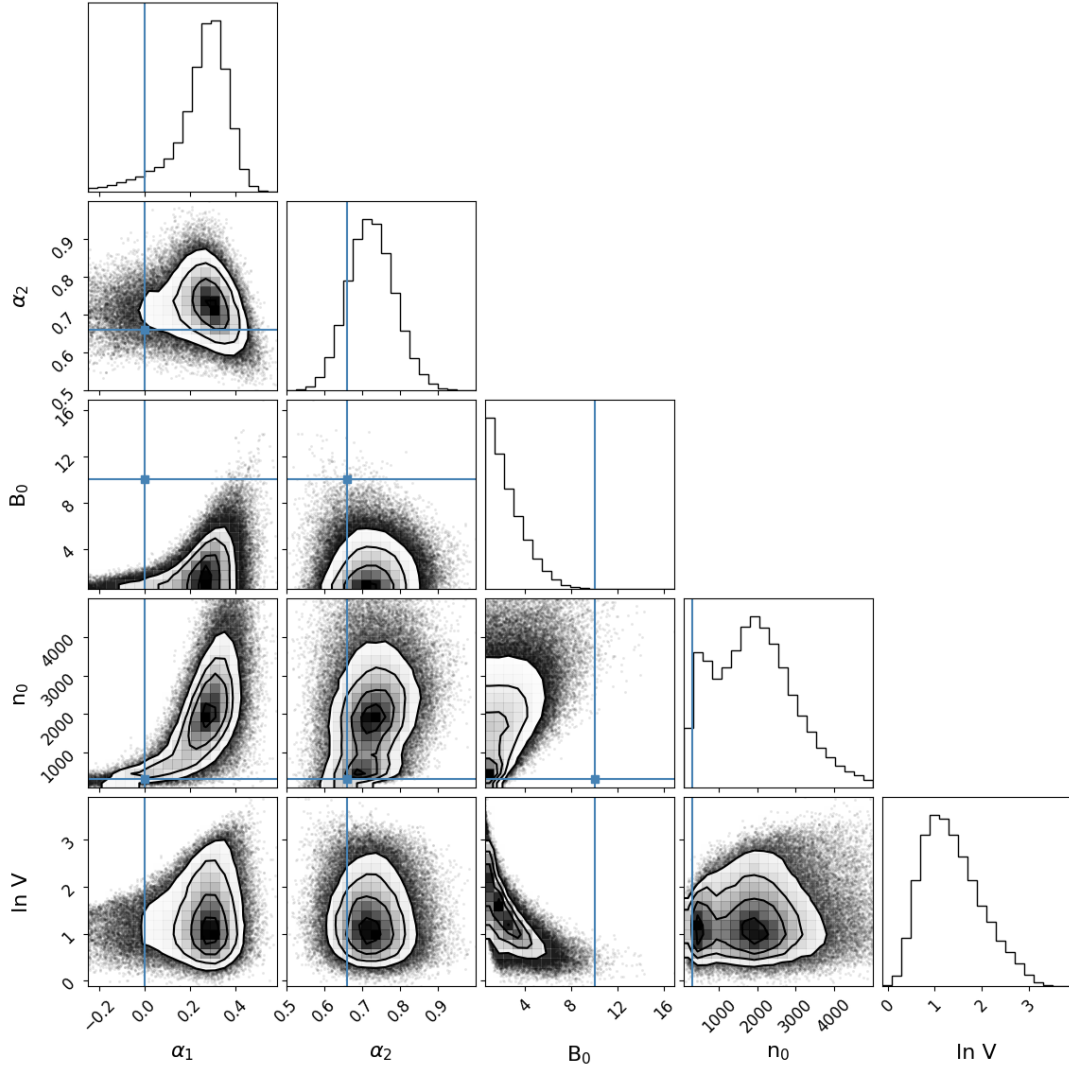
the bimodality that can be seen in the $\ln V - n_0$ plot, the bottom right plot, shows that the MCMC believes there could be two possible relations between $\ln V$ and n_0 . We can also see some bimodality in the $n_0 - \alpha_2$ relationship. What this shows is that the prior assumptions do have an impact on the posterior distributions, thus our analysis is sensitive to the choice of prior. Can we then improve further our assumptions that better represent the information within the data?

Finally, we test a Gaussian plus flat $p(\theta)$. By using a Gaussian distribution of the form $\mathcal{N}(\mu, \sigma)$, where μ is the mean and σ is the standard deviation, we can tell the MCMC that we believe the results are more likely to lie within a physically understandable region of parameter space, but also allow for

it to test outside this region. To set up this prior we set α_1 to the same flat prior used in the previous test. We do this as we have no real prior knowledge of what this exponent will be, other than the tests performed here. For the other parameters we choose to use a Gaussian setting μ to the original values reported in Crutcher et al. (2010) and σ to be broad enough to allow for variation away from the reported values, but not too large that negative values in n_0 and B_0 can arise.

When applying this prior we define three separate $p(\theta)$ to take into account the differences in the data sets. Equation A10 is the prior used for the Zeeman data set, both the line of sight Zeeman (data set 1) and the 3D adjusted data (5) as well as the Scaled (9) and Fiducial (10) data, Equation A11

Data set	α_1	α_2	n_0	B_0	$\ln V$
1	$0.269^{+0.080}_{-0.129}$	$0.723^{+0.063}_{-0.059}$	$1870.825^{+1067.627}_{-1120.618}$	$2.084^{+1.981}_{-1.128}$	$1.282^{+0.738}_{-0.535}$

Table A2. As Table A1 but using the constrained flat PDF in the prior, Equation A9.**Figure A2.** A corner plot for data set 1, Zeeman, using the more constrained flat prior in Equation A9. By looking at the distributions here, the data is better distributed compared to the previous example, but still non-uniform with bi-modality arising in some of the plots, most clearly in the $\ln V$ - n_0 relationship.

is the one used for the reported DCF data from [Pattle et al. \(2022\)](#) (2, 3 and 4) and Equation A12 is the one used for the 3D adjusted DCF data (5, 6, 7, 8). The main difference between the Zeeman and DCF priors is in where B_0 lies. To get a distribution for the DCF data we scaled it down by a factor of 6.3 in line with the average difference between the

Zeeman and DCF data sets reported in [Pattle et al. \(2022\)](#).

$$\begin{aligned}
 p(\alpha_1) &= U(-0.25, 0.75) \\
 p(\alpha_2) &= \mathcal{N}(0.66, 0.25) \\
 p(n_0) &= \mathcal{N}(300, 200) \\
 p(B_0) &= \mathcal{N}(10, 1.5) \\
 p(\ln V) &= \mathcal{N}(1.0, 0.5),
 \end{aligned} \tag{A10}$$

$$\begin{aligned}
p(\alpha_1) &= U(-0.25, 0.75) \\
p(\alpha_2) &= \mathcal{N}(0.66, 0.25) \\
p(n_0) &= \mathcal{N}(300, 200) \\
p(B_0) &= \mathcal{N}(10, 1.5) \\
p(\ln V) &= \mathcal{N}(1.0, 0.5),
\end{aligned} \tag{A11}$$

$$\begin{aligned}
p(\alpha_1) &= U(-0.25, 0.75) \\
p(\alpha_2) &= \mathcal{N}(0.619, 0.056) \\
p(n_0) &= \mathcal{N}(644, 171) \\
p(B_0) &= \mathcal{N}(24, 8.8) \\
p(\ln V) &= \mathcal{N}(0.5, 0.2),
\end{aligned} \tag{A12}$$

We find that the combination of a flat prior for α_1 and Gaussian priors for the other parameters results in a smooth and unimodal estimate of the posterior distribution. The corner plot for the Zeeman data, seen in Figure A3 shows good relationships between each parameter with no large scale scatter. We use this set up for our analysis of the observational data.

For the numerical simulations we use Equation A8. We do this for the large number of simulations we have and that we have to run the MCMC 10 times for each simulation. By using the broad flat PDF we can account for the large data sets, the large variation seen in the data between each simulation and the fact we have no prior knowledge of each simulation. Whilst it would be preferable to have a specific prior distribution for each simulation, for the scope of this study that is computationally unfeasible. We feel confident though that the results we have obtained are robust with how close they match the volume weighted average fit we also plot on the results.

A3 Observational errors

Before running the MCMC using the defined likelihood function and priors we need to address the errors on both the observational data on numerical simulations. Bayesian analysis relies heavily on errors which provide the weighting for each data point. If the data do not have errors then the Bayesian considers those data to be true and will try to force the fit to pass directly through those data, whether they are true data points or not.

A3.1 Errors on the DCF data

The 700 observations compiled by [Pattle et al. \(2022\)](#) come from numerous different instruments including SCUBA and PLANCK. This implies substantial heterogeneity in their error treatments. As we do not have the raw data available to recalculate the errors consistently, we make the approximation that they were all calculated in the same manner. We also, again for simplicity, only include the errors on the values for B . A more robust method would be to also include errors on the number density, but we leave that for future work.

A3.2 DCF- Symmetrical and asymmetrical errors

Only 319 of the 700 observations have reported errors. The ones without errors are mostly in the highest density regime, though they do cover the whole density range. Of the 319 that have errors, 26 of them have asymmetric errors and of those only 5 have a skew of greater than 15%. Again for simplicity we treat these errors as symmetric.

A3.3 DCF - Data lacking errors

For the data that do not report errors we apply symmetric errors derived using the KDE method. This creates a Gaussian distribution of errors as shown in Figure A4. Randomly sampling from this distribution, assuming that it is a good representation of the errors, we apply a symmetric error to each data point lacking errors. Thus, each data point has a reported or approximated symmetric error based on observational results.

A3.4 Errors on the Zeeman data

The Zeeman data from [Crutcher et al. \(2010\)](#) provides line of sight magnetic fields, meaning that we have both positive and negative values of the magnetic-field strength. Whilst this is not an issue for the strength, which can be taken as a magnitude, turning the negative values positive, the treatment of the errors is not as simple. In line of sight space the errors are symmetric and can thus be both positive and negative, but when we take the magnitude of the field strength we run into a problem. If the error is larger than the field strength then the error can return negative values of the magnitude of $|B|$, which is not physically possible. To overcome this we split the field magnitude B into line of sight and plane of sky components such that

$$B^2 = B_z^2 + (B_x^2 + B_y^2)^2 \equiv B_z^2 + B_{\text{pos}}^2, \tag{A13}$$

where B_z and B_{pos} are the line-of-sight Zeeman and plane-of-sky components respectively. If only one component is measured, B can be estimated by assuming that component is the average value over all possible directions (see [Crutcher 2004](#) and [Crutcher et al. 2004](#) for a detailed discussion on this). Note that because B_z is an odd function, we average over its absolute value. Therefore,

$$B = \frac{\pi}{4} B_{\text{pos}} \quad \text{if } B_{\text{pos}} \text{ measured} \tag{A14}$$

$$B = 2|B_z| \quad \text{if } B_z \text{ measured} \tag{A15}$$

If only B_{pos} is measured, and if the measurement uncertainties are normally distributed, then B is also normally distributed with mean and standard deviation $\pi/4$ times the mean and standard deviation of the B_{pos} measurements¹. If only B_z is measured with normally-distributed uncertainties, B is then a **folded normal distribution**. As it is an asymmetric distribution, there is now a nonzero lower bound to the B value for noisy measurements: a measurement $B_z = 0$

¹ While this assumption holds for Zeeman data, according to [Crutcher et al. \(2010\)](#), it may not hold for the plane-of-sky data if computed in a manner similar to the DCF data found in [Pattle et al. \(2022\)](#). We can still use the fact that B will have the same distribution as B_{pos} .

Data set	α_1	α_2	n_0	B_0	$\ln V$
1	$0.307^{+0.129}_{-0.141}$	$0.619^{+0.057}_{-0.055}$	$643.972^{+172.803}_{-169.214}$	$3.813^{+1.551}_{-1.299}$	$0.511^{+0.239}_{-0.206}$
2	$0.262^{+0.018}_{-0.018}$	$0.528^{+0.018}_{-0.018}$	$946.254^{+140.406}_{-142.352}$	$45.160^{+4.186}_{-3.991}$	$0.397^{+0.090}_{-0.085}$
3	$0.259^{+0.018}_{-0.018}$	$0.520^{+0.018}_{-0.017}$	$958.5714^{+140.461}_{-141.857}$	$44.806^{+4.065}_{-3.903}$	$0.392^{+0.088}_{-0.083}$
4	$0.294^{+0.015}_{-0.016}$	$0.411^{+0.011}_{-0.011}$	$529.378^{+138.722}_{-129.501}$	$49.425^{+4.492}_{-4.529}$	$0.226^{+0.058}_{-0.055}$

Table A3. Here we present the results from the testing of the flat + Gaussian prior defined in Equation A10 for the Zeeman data and Equation A11 for the DCF data. We only show the line of sight and plane of sky results here and point to the main body of the work for the full results.

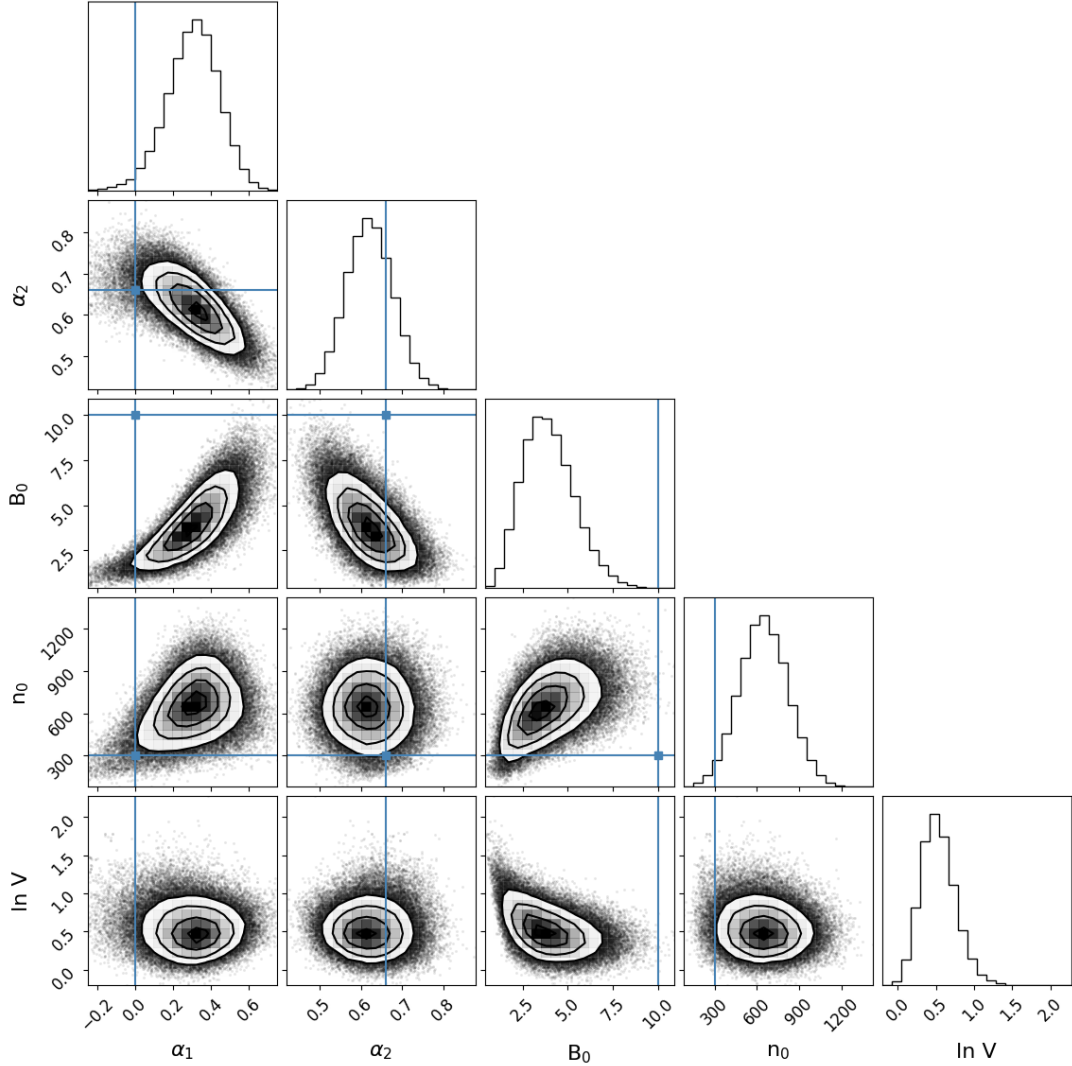


Figure A3. A corner plot for data set 1, Zeeman, using the flat and Gaussian prior defined in Equation A10. We can see here that the distribution is more uniform and unimodal and more evenly distributed in parameter space.

produces a nonzero estimate for B due to the finite noise associated with the measurement. Additionally, the asymmetric distribution also implies that the error bars are no longer symmetric. We then have to compute confidence intervals from the underlying distribution.

Assuming that the factor required to convert measurements into the magnitude B is c , the likelihood function for this

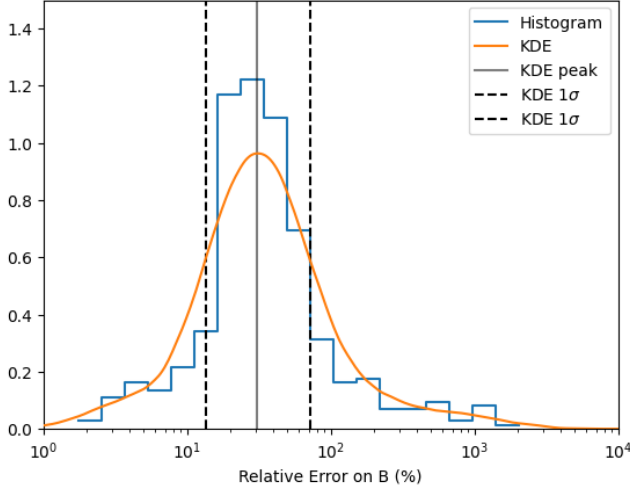


Figure A4. A plot showing the KDE Gaussian distribution (orange line) of the symmetric errors from the DCF data of Pattle et al. (2022) on top of a histogram of the same data. The solid line shows the peak error and the dashed lines show the 1σ spread.

problem, given a data set $\{y_i\}$ with n points, is then

$$\ln p(\theta|\{y_i\}) = -\sum_{i=1}^n \left[\exp -\frac{1}{2} \left(\frac{y_i - y_{mod}(\theta)}{cs_i} \right)^2 + \exp -\frac{1}{2} \left(\frac{y_i + y_{mod}(\theta)}{cs_i} \right)^2 + \ln cs_i \right] + \text{constant}, \quad (\text{A16})$$

where $y_{mod}(\theta)$ and s_i are defined as in Equations A3 and A6 respectively. As before, the latter quantity incorporates a nuisance parameter (see section A1 for more details) to account for unknown systematic errors and intrinsic variance not explained by the measurement errors.

Setting $c = 2$ in Equation A16 is equivalent to applying the conversion factor from Crutcher (2004) for Zeeman to 3-D field strength. If we set it to $c = 1$ we can compute the probability using the errors on the line-of-sight data. We are also able to use this principle when converting the DCF data from plane-of-sky to 3D, using $c = \pi/4$ instead, as described in Crutcher et al. (2004).

One caveat on the method used in this work is that we are assuming all the errors are calculated in the same manner. To treat the errors properly would require each set of observations from a survey or observation to be treated independently with their own nuisance factor. The detail required for that is beyond the scope of this work.

A4 Errors on the numerical simulation data

The numerical data from the various simulations do not include error estimates. Whilst there are various methods of applying errors to the data we choose a simple extension from that used in the observational data for ease. We take the KDE errors calculated from the observational data in Section A3.3 and apply them to the numerical simulations. As with the observational data we combine a nuisance factor with these measurement errors.

A5 MCMC on the numerical data

One issue to overcome with numerical simulations is the size of the data sets. Each simulation consists of well over 5 million points. Running MCMC on such large data sets takes substantial resources. To mitigate the computational cost, we run the MCMC on ten random samples of 50,000 points each from each simulation. We then run the MCMC on each simulation set. The initial conditions for the MCMC analyses are taken from a linear regression fit to the whole data set,

$$(\alpha_1, \alpha_2, n_0, B_0, \ln V) = (0.34, 0.34, 300.0, 10.0, 0.5) \quad (\text{A17})$$

We again take 100 walkers, but due to the large sample of data we reach convergence much faster than with the observational data and so only run for 5000 steps discarding the first 1000 steps and thin to every fifteenth data point.

Once the MCMC has been run we have 10 sets of best-fitting parameter values for each simulation. For each parameter, we compute the median of these ten values and we present them in Table 3. If the errors are symmetric we add them in quadrature, for asymmetric errors we check the difference between them and found that they were all under 10% and therefore add the upper and lower bounds separately in quadrature.

All simulations bar the small and large scale dynamo simulations of Gent et al. (2024) use the same initial conditions as the observational data, as seen in section A1. The reason for the SSD simulations differing is that the data in these diffuse ISM simulations all lie below the values used for the initial condition and so the MCMC is unable to progress as there is no data to constrain it.

For SSD_35 and SSD_98 we set our initial condition to

$$(\alpha_1, \alpha_2, n_0, B_0, \ln V) = (0.0, 0.0, 0.1, 1.0, 0.2) \quad (\text{A18})$$

while for SSD_700 and LSD_3500 we use the initial condition

$$(\alpha_1, \alpha_2, n_0, B_0, \ln V) = (0.34, 0.34, 1.0, 1.0, 0.2) \quad (\text{A19})$$

APPENDIX B: HIGH RESOLUTION MHD SIMULATION OF DWARF GALAXIES

To measure the importance of numerical resolution effects, we re-simulated MHD_10 and MHD_SAT from Whitworth et al. (2023) with higher resolution parameters, Table B1. The new simulations attain r_{cell} resolutions of ≈ 0.01 pc at $n \approx 10^6 \text{ cm}^{-3}$. In the diffuse gas, $n \approx 10^{-2} - 10^0 \text{ cm}^{-3}$ the cell resolution is below ≈ 10 pc, similar to the resolution of the densest gas in the RAMSES Milky Way like simulations. The new base gas mass in the cells is set to 1 M_\odot and allowed to vary by a factor of 2 and further refined to resolve the Jeans length, which is set to 8 cells. The accretion radius around the sink particles is reduced to 0.01 pc. The maximum mass that a sink is allowed to grow to is set at 1000 M_\odot , allowing for massive star formation. We have also included the effects of photoionization. The method implemented here is described in Whitworth et al. (2024). The new simulations are run for 10 Myr from the 1 Gyr snap of the original simulations to allow for the new resolution to take effect, a new population of sink particles to have formed, and ensure that no large-scale changes in the behaviour or growth of the magnetic field have arisen (see Fig. B2).

ρ_c (g cm $^{-3}$)	2.4×10^{-19}
n (cm $^{-3}$)	10^5
r_{acc} (pc)	0.01
Softening Length (pc)	0.10
Max sink mass (M_\odot)	1000
Base cell mass (M_\odot)	1

Table B1. Sink particle and resolution parameters used for the new AREPO MHD simulations. ρ_c is the sink density threshold, n (cm $^{-3}$) is the number density of the sink threshold, r_{acc} is the accretion radius, the softening length is the adaptive gravitational softening length of the gas cells, the base cell mass is the target mass of the cell which is allowed to vary by factor of 2.

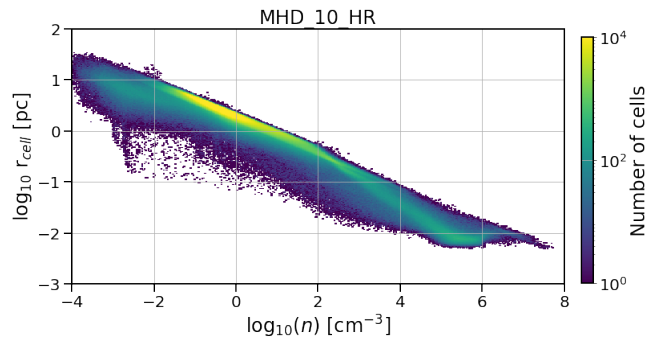


Figure B1. The cell resolution of simulation MHD_10_HR where we can see the sub-parsec resolution being around number densities of $\sim n = 1 \text{ cm}^{-3}$.

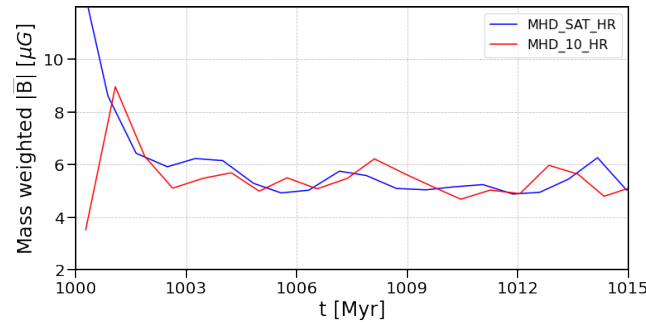


Figure B2. The mass-weighted absolute magnetic field strength in simulations MHD_10_HR and MHD_SAT_HR taken from within a radius of 1.5 kpc and $z = \pm 0.2$ pc. We see no change in the field strength over the 15 Myr of the new simulations. The peak at the beginning is from the code refining the gas to the new levels.

APPENDIX C: THE DIFFUSE GAS PHASE

Does the behaviour of the field change when we better resolve the diffuse gas? We compare the plasma $\beta = P_{\text{thermal}}/P_{\text{mag}}$, where $\beta < 1$ means magnetic pressure dominates over thermal pressure, and the Alfvénic Mach number $\mathcal{M}_A = \langle v^2/v_A^2 \rangle^{0.5}$, where if $\mathcal{M}_A < 1$ then the magnetic field dominates the turbulent flow.

Figure C1 shows the difference between the simulations in the plasma- β where it can be seen that at the high densities the field is dominant over thermal pressure. At lower densities

it is a little less clear. To be able to see the change we looked at the mass fraction of gas below a plasma- β below 1 and compare between the simulations. There is no change in the gas mass fraction below $n = 300 \text{ cm}^{-3}$ and a plasma- $\beta < 1$. However when we look at $n \leq 1 \text{ cm}^{-3}$ the gas mass increases by a factor of 2.85 for MHD_10 and a factor of 0.38 for MHD_SAT.

What about \mathcal{M}_A ? Figure C2 shows a comparison between the new simulations (top row) and the original simulations (bottom row). Here we can see that in the low density gas the field is only slightly more dominant, more so in MHD_SAT_10. But as the bulk of the gas is still above $\mathcal{M}_A = 1$ the overall effect is minimal.

So there is a very slight change in the behaviour of the diffuse gas when we are able to better resolve it. Why is this? In these simulations the field is supported and grown by the turbulent SSD and the LSD. In the diffuse gas the dynamo won't be properly resolved if the gas is also not resolved. The stretch-twist-fold of the field lines that occurs on small, sub-parsec scales won't be modelled correctly. Work has shown (Gent et al. 2021) that resolution affects the speed of growth of the field, so in an unresolved diffuse medium the field will grow slower than in a resolved medium. Numerical simulations tend not to resolve the diffuse medium for computational efficiency. Galaxy evolution simulations also tend to not consider the diffuse medium as important as no star formation takes place there. However, if the magnetic field in the diffuse medium is important, then we need to resolve this better as it will slow down accretion onto giant molecular clouds, slowing their growth. A more thorough examination of the effects of magnetic fields on the diffuse ISM is beyond the scope of this work, but would provide invaluable insights.

A quick test of whether this translates to a change in the velocity dispersion of the gas may give some insight. Figure C3 would seem to suggest there is little change except at extremely low number densities and $|\vec{B}|$ where the cells are largest and we have lost resolution. At number densities where \mathcal{M}_A is super-Alfénic, $n = 10^{-2} - 10^0 \text{ cm}^{-3}$, there is little to no change in σ_v between the simulations. Radially there is a slight increase in σ_v in MHD_SAT_HR but not significant enough to make a drastic change. And when compared to the strength of the field again we see very little variation.

This paper has been typeset from a *T_EX/L_AT_EX* file prepared by the author.

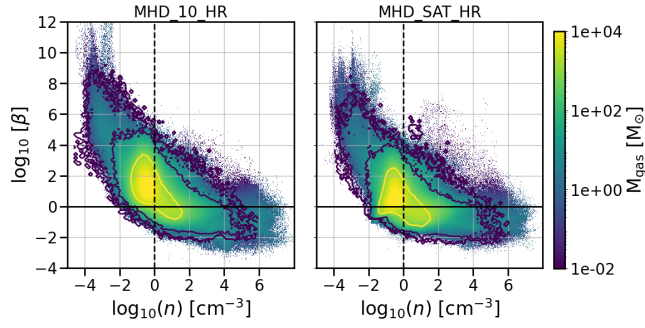


Figure C1. Plasma β versus number density for MHD_10_HR and MHD_SAT_HR. The contours show the same but for simulations MHD_10 and MHD_SAT. The *black horizontal line* shows plasma- $\beta = 1$. Below this magnetic pressure dominates over thermal pressure. In the denser regions, represented by the *black vertical dashed line* at $n = 1 \text{ cm}^{-3}$, we see more gas that is magnetically dominated. In the low density gas there is no clear difference.

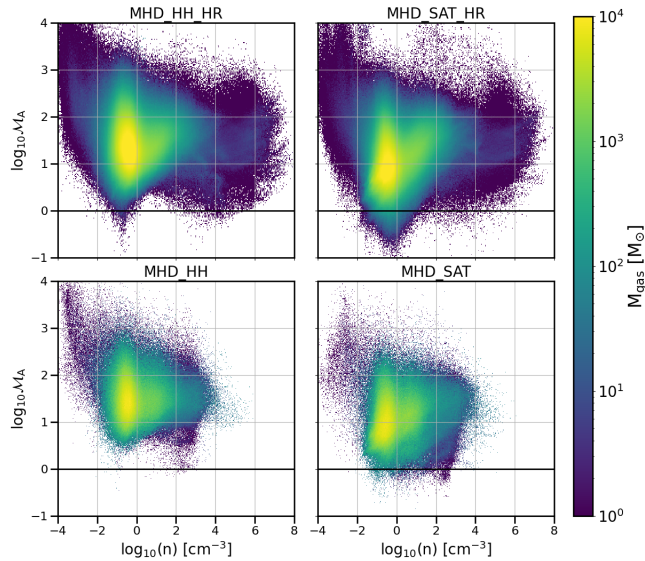


Figure C2. The Alfvénic Mach number for simulations MHD_10_HR and MHD_SAT_HR (top row) and MHD_10 and MHD_SAT (bottom row). The *black horizontal line* represents $\mathcal{M}_A = 1$. Below this line magnetic turbulence dominates and above gravitational turbulence is dominant. We can see that in the high resolution simulations, below number densities of $n = 1 \text{ cm}^{-3}$ there is more gas below $\mathcal{M}_A = 1$ showing the magnetic field becoming more dominant there.

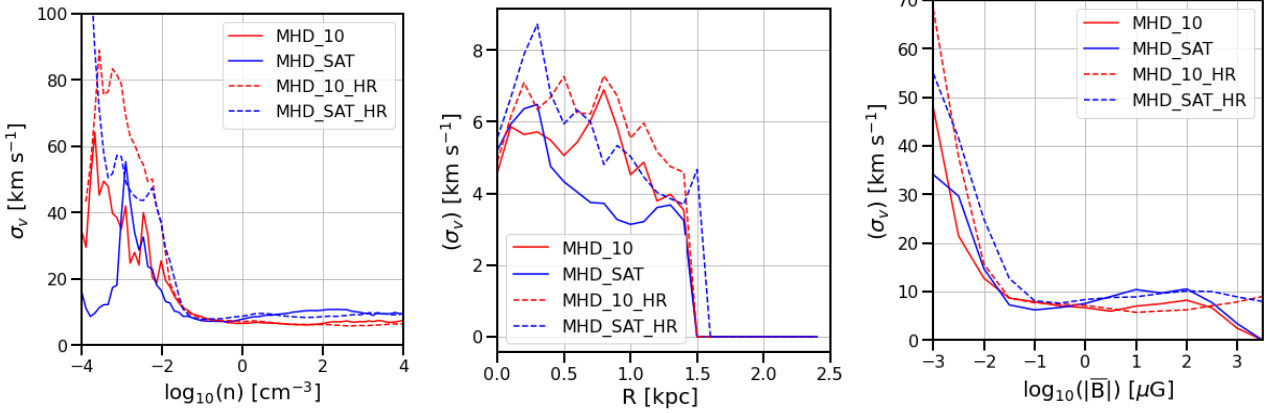


Figure C3. The mass-weighted velocity dispersion (σ_v) for simulations MHD_10_HR (red) and MHD_SAT_HR (blue):dashed lines, and MHD_10 (red) and MHD_SAT (blue):solid lines. The left panel shows σ_v versus number density (n), the middle pannel shows the radial distribution and the right is versus absolute magnetic field strength ($|\bar{B}|$). We can see that in the low field ($|\bar{B}| < 10^{-1}$) and low number density ($n = 10^{-2}$ cm $^{-3}$) regime the σ_v is much larger. This increase in velocity dispersion is not related to the knee in the Crutcher relation, but appears at much lower n and $|\bar{B}|$.